UNIVERSITY OF CALIFORNIA SAN DIEGO

Santa Ana Winds of Southern California: Historical Variability and Future Climate Projections.

A dissertation submitted in partial satisfaction of the
requirements for the degree

Doctor of Philosophy

in

Earth Sciences

by

Janin Guzman Morales

Committee in charge:

Alexander Gershunov, Chair
Tereza Cavazos
Daniel R. Cayan
Raymond de Callafon
Amato T. Evan
Gabi Laske
Joel R. Norris

2018

Copyright

Janin Guzman Morales, 2018

All rights reserved

The Dissertation of Janin Guzman Morales is approved, and it is acceptable in quality and form for publication on microfilm and electronically:

_____

_____

_____

_____

_____

_____

_____

_____
Chair

University of California San Diego

2018

DEDICATION

To my father, whose love has followed me through all my endeavors.

And to every person that has crossed the border.

TABLE OF CONTENTS

LIST OF ABBREVIATIONS

ASOS	Automated Surface Observing System station
CC	Canonical Correlate
CaRD10	California Reanalysis Downscaling to 10 km
CCA	Canonical Correlation Analysis
CBR	California Border Region
CMIP3	Coupled Model Intercomparison Project Phase 3
CMIP5	Coupled Model Intercomparison Project Phase 5
ENSO	El Niño-Southern Oscillation
EOF	empirical orthogonal function
FWI	Fire Weather Index
GCM	Global Climate Model
MSM	Mesoscale modelling
NRMSE	normalized root-mean-squared error
PGF	Pressure gradient force
PDO	Pacific Decadal Oscillation
PC	principal component
PCA	principal component analysis
RAWS	Remote Automated Weather Stations
R1	NCEP/NCAR Reanalysis 1
R1D	NCEP/NCAR Reanalysis 1 statistical downscaling
SAWs	Santa Ana Winds
SAWRI	SAW Regional Index

SD	Statistical Downscaling
SLP	Sea Level Pressure
SoCal	Southern California
SOS	Skill Optimization Surface
WF	Witch Creek Fire
WUI	wildland-urban-interface

LIST OF FIGURES

LIST OF TABLES

ACKNOWLEDGEMENTS

First and foremost, I am deeply thankful to my advisor Alexander Gershunov whose guidance and insights through this process has been fundamental and invaluable. I'm indebted to my advisor for his dedication to the success of this dissertation and for the years of mentorship and friendship. In this world of infinite possibilities my experience as a graduate student in his research group, has been a luminous experience professionally and personally. I am in debt with him.

My special thanks to my research group, Rachel Clemesha, Tamara Shulgina, and Kritsten Guirguis for the vibrant intellectual community that has kept my laboratory environment a collaborative and supportive space.

Dan Cayan, David Pierce for helping me with statistical downscaling and expanding the scope of my research.

My committee: Dan Cayan, Tereza Cavazos, Joel Norris, Amato Evan, Gabi Laske, and Raymond de Callafon for serving as my committee and the multiple suggestions and feedback that propelled this dissertation forward.

Chapter 1, in full, is a reprint of the material as it appears in *Geophysical Research Letters* in 2016, with slight modifications. Guzman-Morales, J., Gershunov, A., Theiss, J., Li, H., & Cayan, D. (2016). Santa Ana Winds of Southern California: Their climatology, extremes, and behavior spanning six and a half decades. *Geophysical Research Letters*, *43*(6), 2827–2834. https://doi.org/10.1002/2016GL067887 ©American Geophysical Union. Used with permission. The dissertation author was the primary investigator and author of this paper.

Chapters 2 and 3, in full, will be soon submitted for publication to *Geophysical Research Letters*, with slight modifications. Guzman-Morales, J., and Gershunov, A. (2018). Climate Change Suppresses the Santa Ana Winds of Southern California and Sharpens their Seasonality. *Submitted for publication in GRL*. The dissertation author was the primary investigator and author of this paper.

VITA

2010 B.S. in Chemistry, National Autonomous University of Mexico.

2011 Grantee of the CONACyT-UCMEXUS Doctoral Fellowship

2018 Ph.D. in Earth Sciences, University of California San Diego

PUBLICATIONS

Guzman-Morales, J., and Gershunov A. (2018). Climate Change Suppresses the Santa Ana Winds of Southern California and Sharpens their Seasonality. *In preparation.*

Guirguis, K., Basu, R., Al-Delaimy, W. K., Benmarhnia, T., Clemesha, R. E. S., Corcos, I., **Guzman-Morales, J.,** Small, I., Tardy, A., Vashishtha, D., Zivin, J. G., & Gershunov, A. (2018). Heat, Disparities, and Health Outcomes in San Diego County's Diverse Climate Zones. *GeoHealth*. https://doi.org/10.1029/2017GH000127

Syphard, A.D., Gershunov, A., Lawson, D.M., Rivera Huerta, H., **Guzman-Morales, J.**, and Jennings, M.K.. 2018. San Diego Wildfires: Drivers of Change and Future Outlook. Pages xx - xx in: Jennings, M.K., D. Cayan, J. Kalansky, A.D. Pairis et al. San Diego County Ecosystems: Ecological Impacts of Climate Change on a Biodiversity Hotspot. California's Fourth Climate Change Assessment, California Energy Commission. Publication number: EXT-CCC4A-2018-XXX. D

Guzman-Morales, J., Gershunov, A., Theiss, J., Li, H., & Cayan, D. (2016). Santa Ana Winds of Southern California: Their climatology, extremes, and behavior spanning six and a half decades. *Geophysical Research Letters*, *43*(6), 2827–2834. https://doi.org/10.1002/2016GL067887

Guzman-Morales, J., Frossard, A. A., Corrigan, A. L., Russell, L. M., Liu, S., Takahama, S., Taylor, J.W., Allan, J., Coe, H., Zhao, Y., & Goldstein, A. H. (2014). Estimated contributions of primary and secondary organic aerosol from fossil fuel combustion during the CalNex and Cal-Mex campaigns. *Atmospheric Environment*, *88*. https://doi.org/10.1016/j.atmosenv.2013.08.047

Takahama, S., Johnson, A., **Guzman Morales, J.,** Russell, L. M., Duran, R., Rodriguez, G.,Zheng, J., Zhang, R., Toom-Sauntry, D., & Leaitch, W. R. (2013). Submicron organic aerosol in Tijuana, Mexico, from local and Southern California sources during the Calmex campaign. *Atmospheric Environment*, *70*. https://doi.org/10.1016/j.atmosenv.2012.07.057

ABSTRACT OF THE DISSERTATION

Santa Ana Winds of Southern California: Historical Variability and Future Climate Projections.

by

Janin Guzman Morales

Doctor of Philosophy in Earth Sciences

University of California San Diego, 2018

Alexander Gershunov, Chair

Santa Ana Winds of Southern California and Northern Baja California (SoCal) are the primary weather drivers of wildfires that frequently and infamously ravage this topographically and demographically complex region. As the available wind observations are scarce, Santa Ana Winds (SAWs) have not been adequately studied on climate timescales. Yet, wildfire behavior has been changing wildly even during my dissertation work. For example, the largest wildfire in California's recorded history occurred in December of 2017, well outside the unique fall season for the largest wildfires typical of this region. This dissertation presents results of my efforts to understand Santa Ana wind behavior on climate timescales and in our changing climate. In Chapter 1, I developed and analyzed the longest and most complete record of hourly SAWs heretofore available. These results provide a

robust perspective on both high- and low-frequency SAW behavior, uncovering previously unknown climate influences on SAW activity, and laying the groundwork for eventual studies into seasonal SAW predictability. Notably, the 65-year record of hourly SAWs did not manifest clear long-term trends. In Chapter 2, using a dynamically downscaled training data set, I developed an approach to statistically downscale coarsely resolved winds from a global Reanalysis with spatial resolution typical of global climate models (GCMs). The result was an efficient and skillful downscaling of coarse daily surface wind vectors onto a fine grid over the SoCal domain spanning 70 years. From these daily wind fields, I derived SAWs and validated them against my previously validated SAWs derived in Chapter 1 from our dynamical training data set. A capacity to statistically downscale daily winds from reanalyses and global climate models was thus developed and applied, in Chapter 3, to a set of eight GCMs yielding an ensemble of daily 10X10 km wind data sets covering SoCal and spanning a historical and future projected time period from 1950 to 2100. Analyses of these data yielded physically meaningful, robust and clear projections of SAW activity gradually decreasing and constricting around its traditional seasonal peak centered on December. These results provide robustness, nuance and meteorological context to expectations of future SoCal wildfire activity.

Chapter 1

Santa Ana Winds of Southern California: Climatology, extremes and behavior spanning six and a half decades

Santa Ana Winds (SAWs) are an integral feature of the regional climate of Southern California/Northern Baja California region, but their climate-scale behavior is poorly understood. In the present work, we identify SAWs in mesoscale dynamical downscaling of a global reanalysis from 1948 to 2012. Model winds are validated with anemometer observations. SAWs exhibit an organized pattern with strongest easterly winds on westward-facing downwind slopes, and muted magnitudes at sea and over desert lowlands. We construct hourly local and regional SAW indices, and analyse elements of their behavior on daily, annual, and multi-decadal timescales. SAWs occurrences peak in winter, but some of the strongest winds have occurred in fall. Finally, we observe that SAW intensity is influenced by prominent large-scale low-frequency modes of climate variability rooted in the tropical and north Pacific ocean-atmosphere system.

1.1 Introduction

SAWs are episodic pulses of easterly, downslope, off-shore flows over the coastal topography of the California Border Region (CBR): Southern California and Northern Baja California. SAWs represent a distinct and common regional cool season weather regime, a reversal of the typical wintertime on-shore winds, contrasted with northwesterly alongshore and on-shore flow characteristic of summer (Conil & Hall, 2006). SAWs are associated with very dry air, often with anomalous warming at low elevations, and produce strong gusty

downslope winds concentrated in gaps and on the lee slopes of the coastal ranges, e.g. Santa Ana, Santa Monica, and Laguna Mountains.

It is in these rugged hills and canyons, after long dry summers characteristic of this Mediterranean climate, that SAWs can drive catastrophic wildfires that CBR is infamous for (Boyle, 1995; Westerling et al., 2004; Moritz et al., 2010). SAWs fanned the October 2007 wildfires that killed nine people, injured 85 others including 61 fire-fighters, and destroyed upwards of 1,500 homes, scorching 2,000 km² of land on the U.S. side of the border alone. The October 2003 SAW-fanned wildfires were even more extensive. Wind-blown smoke inhalation from these 2003 wildfires in Southern California resulted in 69 premature deaths, 778 hospitalizations, 1431 ER visits and 47K outpatient visits (Delfino et al., 2009). More recently, the rare May 2014 events fanned extraordinarily late-season fires following an extremely dry winter. Moreover, early and late season SAWs drive coastal heat waves, one reason why early fall rather than summer is historically the season for the hottest temperature extremes along the coast (Gershunov & Guirguis, 2012). In spite of their tremendous episodic impacts on the health, economy and mood of the region, a direct wind-based, long-term, and high-frequency climatology of SAWs is not available and relationships with larger-scale climate variability have not been clearly elucidated. This article begins to address these knowledge gaps for SAW behavior.

Indirect or proxy-based climatologies of SAWs have been typically diagnosed from synoptic-scale information. Raphael (2003) diagnosed 33 years of daily SAWs from observed pressure fields, while Jones et al. (2010) diagnosed 28 years of daily Fire Weather Index (FWI, Fosberg, 1978) values, of which dry winds are a component, derived from the North American Regional Reanalysis (Mesinger et al., 2006). Abatzoglou et al. (2013)

developed the longest empirical daily reconstruction to date, from 1948 to 2012 based on pressure fields and temperature advection from global reanalysis.

Mesoscale modelling (MSM) has also been employed in the study of SAWs, typically to investigate the anatomy of SAWs from small samples of individual events (e.g. Sommers, 1978; Lu et al., 2012; Moritz et al., 2010) provided a longer perspective using a decade of SAWs dynamically downscaled, and demonstrated the ability to predict large observed wildfire locations via model-derived FWI. Other studies have also employed MSM data sets spanning up to a decade with high spatio-temporal resolution to characterize SAWs among Southern California's regional weather regimes (Conil & Hall, 2006) and to investigate their causal mechanisms (Hughes & Hall, 2010). Following on this work, Hughes et al. (2011) investigated anthropogenic climate change impacts on SAWs.

Here, we use mesoscale-modeling-derived wind data exclusively to define and quantify a long record of observationally-validated SAWs. In what follows, we use observed wind to validate hourly winds in a 65-year dynamical downscaling of a global reanalysis to 10km. We develop and apply a SAW definition with locally specific wind thresholds and, after determining their canonical spatial footprint, we define a SAW Domain, from which is constructed a SAW Regional Index. Subsequently, we examine the SAW climatology, paying particular attention to extremes, noteworthy events, interannual and longer-term variability. We finally discuss results in the context of regional climate variability, predictability and change, and in terms of their relevance to wildfire.

1.2 Data and Methods

1.2.1 CaRD10 Modeled Winds

To examine SAW variability in space and time, we use winds from the California Reanalysis Downscaling to 10 km, CaRD10 (Kanamitsu & Kanamaru, 2007). CaRD10 is a dynamical downscaling of the NCEP/NCAR Reanalysis 1 (R1, Kalnay et al., 1996) that employs the Regional Spectral Model, RSM (*Kanamitsu et al.*, 2005)], a mesoscale counterpart of the Global Spectral Model that produced R1. RSM provides instantaneous winds at 10 m above the ground in hourly resolution from 1948 through 2012. The CaRD10 dataset is the longest mesoscale record to date and its downscaling system, validation, and comparison with the North America Regional Reanalysis are reported in a two-part paper by Kanamitsu & Kanamaru (2007) and Kanamaru & Kanamitsu (2007). Our domain extends from (118.115˚W, 35.081˚N) at the NW point to (116.035˚W, 32.053˚N) at the most SE point with a total of 756 grid cells (21 × 36). This domain captures the core of the CBR extending 65 km across the border into Northern Baja California, Mexico (Figure 1.1).

1.2.2. Sustained Wind and Wind Gust Observations

Southern California is comparatively rich with anemometer measurements (Horel & Dong, 2010) that have been underutilized for SAW research. Arguably, available observations are not of sufficient length and/or density to adequately resolve long-term variability and topographic effects, but they provide useful local and regional validation of modeled winds. Kanamitsu & Kanamaru (2007) demonstrated that CaRD10 winds over the coastal North Pacific Ocean were closely related to observed winds at selected ocean buoy locations. Here, focusing on the terrestrial region where SAWs are most prevalent, CaRD10 model skill is tested against sustained wind (wind speed average) and wind gust (maximum "instantaneous" wind speed) observations from 85 Remote Automated Weather Stations

(RAWS), and one Automated Surface Observing System station (ASOS) across the domain (shown in Figure 1.1). The specific operational definitions of sustained winds and wind gust used by ASOS and RAWS can be found at http://www.nws.noaa.gov/asos/aum-toc.pdf, and http://raws.fam.nwcg.gov/nfdrs/pms426-3.pdf, respectively.

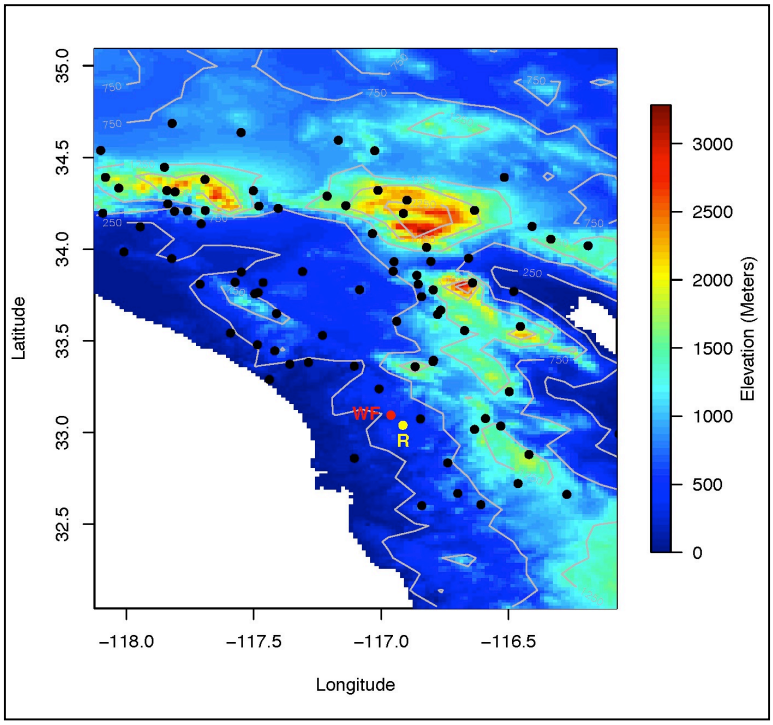

Figure 1.1. Spatial domain of the CBR with topography. Elevation is shown at 60 arc-second (colors), and 10-km spatial resolution (contours). Black dots mark the location of RAWS, and yellow dots show ASOS at Ramona Airport labeled "R". Location of Witch Creek Fire (WF) start in late October 2007 is shown as a red dot.

1.2.3 Validation

Stations are matched with the closest grid cell of the CaRD10 domain. For each grid cell-station pair, correlation coefficient (r) and normalized root mean squared error (NRMSE) are calculated for the overlapping part of the station and CaRD10 records. The normalization factor is the difference between the maximum and minimum observations

across all stations. To scrutinize model performance during SAWs, we recalculate *r* and NRMSE values only for periods regarded as experiencing local SAW conditions (section 1.2.4).

Correlations between CaRD10 winds and observed sustained winds are generally positive, but have modest strength, ranging between 0.13 and 0.64. Actually, the CaRD10 winds correlate more strongly with gusts than sustained winds at 78 (91% of) stations. This consistently stronger link with observed gusts is seen on the histograms shown on Figure 1.2a,b. Errors, measured as NRMSE, against gusts are also consistently smaller than errors against sustained winds (Figure 1.3a,b); this is the case at 65 (76% of) stations. When using SAWs only, correlations at some stations improve but deteriorate at others (see flatter histograms on Figure 1.2c-d compared to a-b). However, the agreement between modeled SAWs and observations still consistently favors observed gust over sustained wind (Figure 1.2c-d, and 1.2c-d).

Modeled winds are instantaneous, neither sustained nor gust. Modeled winds overestimate sustained near-surface winds. Beyond possible model biases, part of the reason for this may be that observed winds are affected by fine scale orography, particularly in complex terrain, surface roughness, as well as obstructions around the anemometer, not resolved by the model. Gusts are less sensitive to such features as they are more related to the flow above the boundary layer via turbulent mixing (Brasseur, 2001). Supporting this notion, CaRD10 SAWs appear to validate best with gusts observed at high elevation stations (Figure 1.2d) where SAWs are strong and gusts are more directly related to the flow above the shallow boundary layer, which also drives CaRD10 10m winds via boundary layer parameterization. Clearly, whether due to model and/or observational biases, and although

the dynamical model does not simulate gusts, modeled winds are a most accurate approximation of observed gusts. In other words, on average over our domain, CaRD10 winds overestimate sustained winds by a factor of about 2.3, which happens to be about equal to the average ratio of wind gust to sustained wind speed, i.e, the space-time average gust factor.

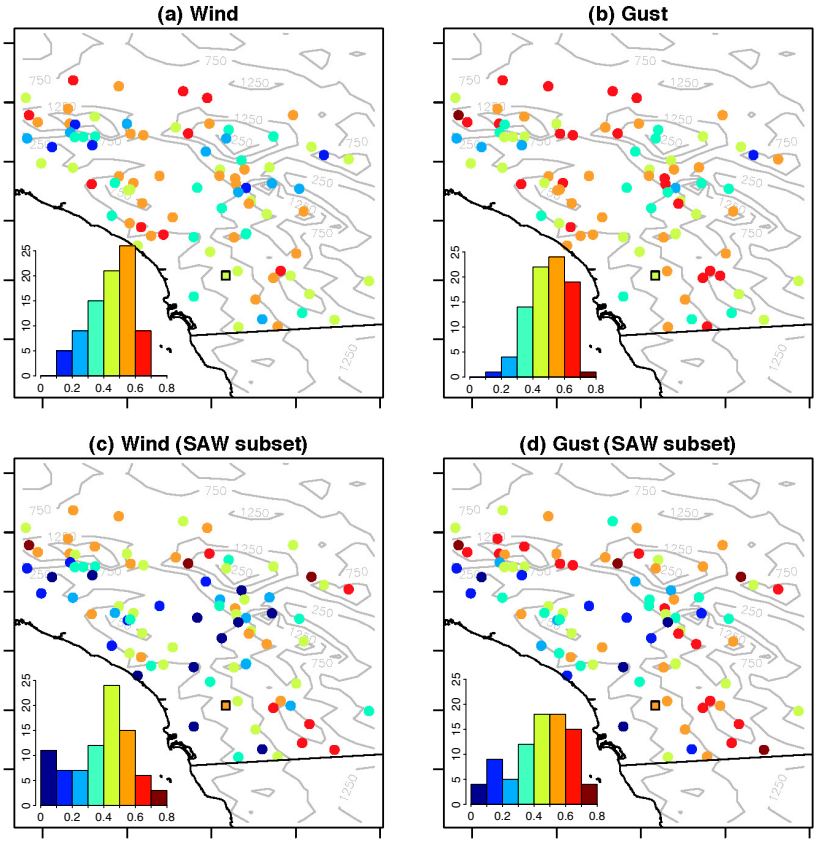

Figure 1.2. Correlations (*r*) of hourly CaRD10 winds with observations at RAWS (circles) and ASOS station at Ramona Airport (square). Top panels show the correlations with sustained wind (a) and gust (b). Bottom panels show the correlation of selected SAWs with also sustained winds (c) and gust (d). The histograms depict the number of stations per correlation intervals of 0.1.

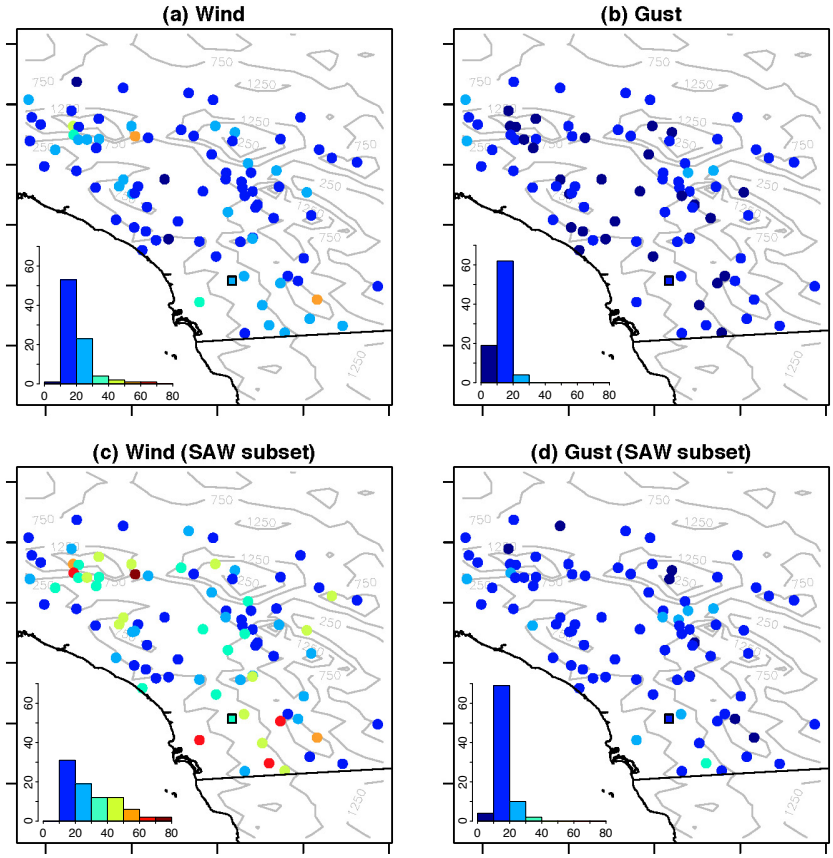

Figure 1.3. Normalized root mean squared errors (NRMSEs) of hourly CaRD10 winds against observations at RAWS (circles) and ASOS station at Ramona Airport (square). Top panels show the NRMSEs with sustained wind (a) and gust (b). Bottom panels show the NRMSEs of selected SAWs with sustained winds (c) and gust (d). The histograms depict the number of stations per NRMSE interval of 10%.

1.2.4 Local Definitions of Santa Ana Winds

Modeled strong winds tend to converge between easterly and notheasterly directions with surface relative humidity dropping into single digits (Figure 1.4). This behavior suggests that wind direction and speed are sufficient to define SAWs. At each grid cell or station, we first identify winds with directions > 0˚ and < 180˚ (winds with a negative u component), and define local speed thresholds as the upper quartile of the direction-selected

winds. Periods with at least 12 hours of continuous selected winds that exceed the local wind speed threshold for at least one hour are defined as SAWs. Discontinuities are allowed for periods of 12 hrs or less, to allow for breaks in SAW events, e.g. competing afternoon sea breeze episodes. The resulting SAW index reflects the full wind speed during periods that fulfil the direction-continuity scheme.

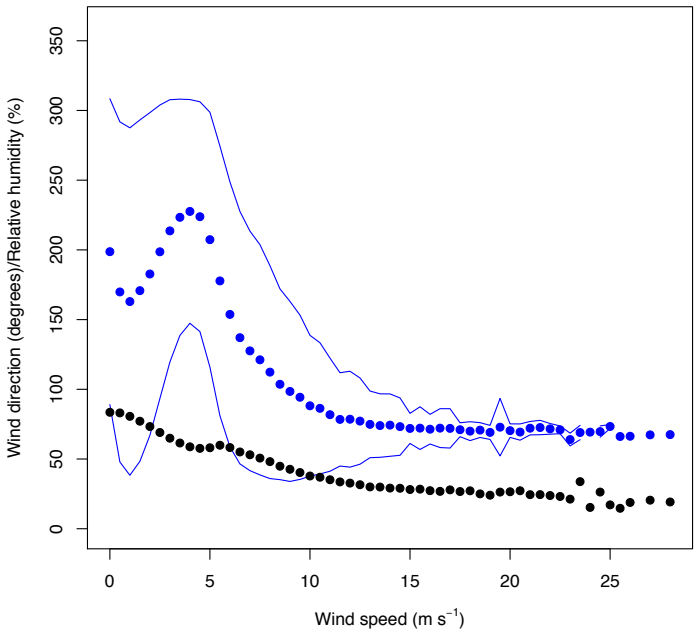

Figure 1.4. Mean wind direction in degrees as a function of wind speed binned in 0.5 m s^{-1} intervals (blue dots) with 95% confidence interval (blue lines) for the 65-year record at Ramona. Degrees are counted clockwise from North (90 is Easterly). Average relative humidity as a function of wind speed is also shown for the same bins (black dots) on a shared y-axis where 100, instead of angular direction, denotes 100% relative humidity.

Ramona, California (Figure 1.1), located in west-facing foothills of the Laguna Mountains, is known to be a windy fire-prone location where the late October Cedar Fire (2003) and Witch Creek Fire (2007) burned during severe multiple wildfire episodes. In this

work, we turn to Ramona for local examples. The correlation for the whole period of available gust and sustained wind observations (from 2005 to 2010) with Ramona SAW is 0.7 and 0.6, respectively. Figure 1.5b, shows the excellent agreement between SAW and observed gust at Ramona, during early-season SAW events of 2007 and 2010.

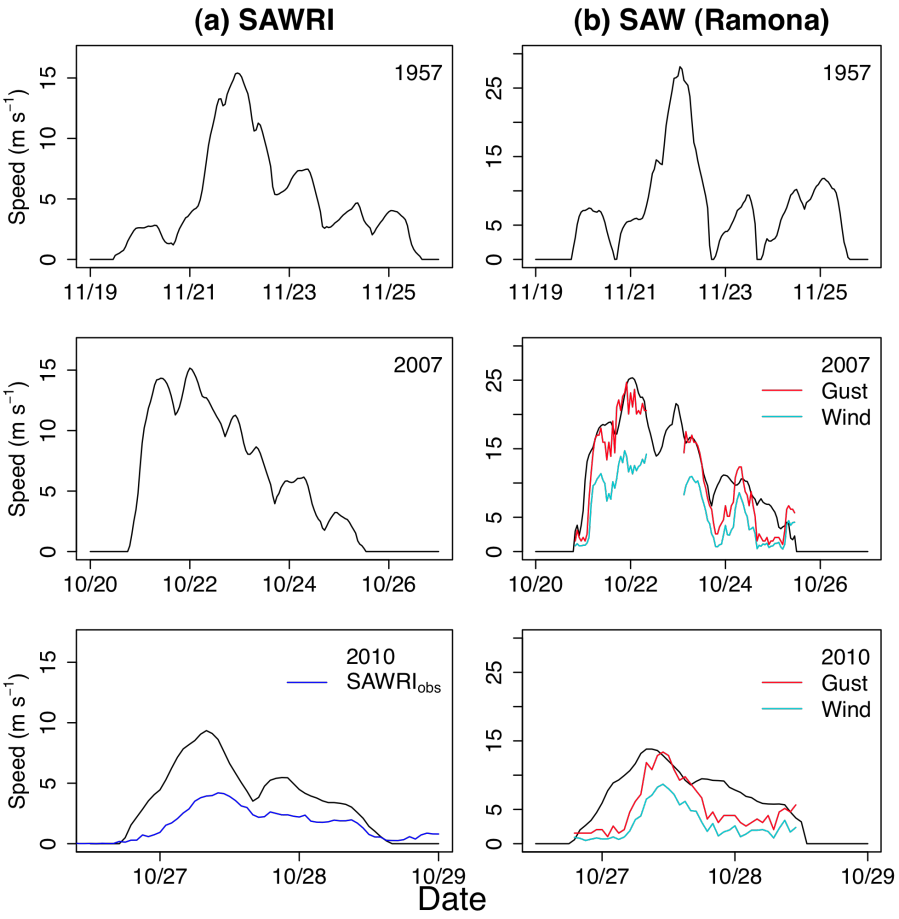

Figure 1.5. Regional and local indices of early-season SAW events. (a) Hourly SAWRI of events in 1957, 2007, and, 2010. SAWRI from observations is available for the 2010 event. (b) Hourly SAWs at Ramona for the same events as in (a). Hourly sustained wind and gust from Ramona Airport ASOS station are available and shown for 2007 and 2010 events.

1.2.5 Regionalizing Local SAWs

We examine the spatial and seasonal coherence of locally defined SAWs. In the CaRD10 dataset, the strongest SAWs are found on downwind slopes of the main topography,

while SAWs relative to other winds reflect an almost identical pattern (Figures 1.6a,b) with comparatively lower values at sea, and lowest values over the desert basins. This SAW-speed spatial distribution is notably consistent with Hughes & Hall (2010) who determined it to be forced by katabatic acceleration of cool air downslope as well as downward momentum transfer.

We calculate the empirical orthogonal functions (EOFs) of hourly SAWs. The leading principal component (PC1) explains 50% of the total hourly SAWs variance over the region and its time series corresponds to SAW seasonality (Figure 1.7a). Broad regional coherence of SAW selection is displayed as correlations of PC1 with SAWs time series (Figure 1.6c). We also quantify the regional concurrence of SAWs across the domain with Ramona SAWs (Figure 1.6d), noting that SAWs at selected locations are well represented by the regional aggregate SAW index (described below).

Consistent with the above results, we define the SAW Domain as the region displaying coherent SAWs in time and magnitude, Thus, the SAW Domain is explicitly constrained to grid cells where PC1 explains 50 % of the variance, i.e. where correlations between SAWs and PC1 exceed 0.7, and by high wind speed ratios (>1.5). For the sake of continuity, we include the low-ratio cluster of grid cells northeast of the Santa Ana Mountains and adjacent ocean-grid cells (~40 km off-shore). SAW Domain covers 43% of the original domain (Figure 1.6).

The SAW Regional Index (SAWRI) is then defined as the hourly average of the SAWs across all the grid cells within the SAW Domain. Hourly SAWRI is correlated with PC1 at r =0.9 and with Ramona SAWs at r = 0.7. We reconstruct two seasons of observed SAW Regional Index ($SAWRI_{obs}$) from the stations wind observations, see Annex 1A for

details. The correlation between the hourly SAWRI and $SAWRI_{obs}$ is 0.6. Comparison at different temporal resolutions is shown in Figure 1.7.

SAW events are directly quantified by continuous periods of SAWRI and classified into three categories according to their maximum SAWRI – weak (< 5 m s^{-1}), moderate (5 - 10 m s^{-1}), and extreme (10 -15 m s^{-1}) –. Extremes events are above the 90th percentile of all events on record. Finally, we integrate SAWRI over time to obtain total seasonal SAW activity.

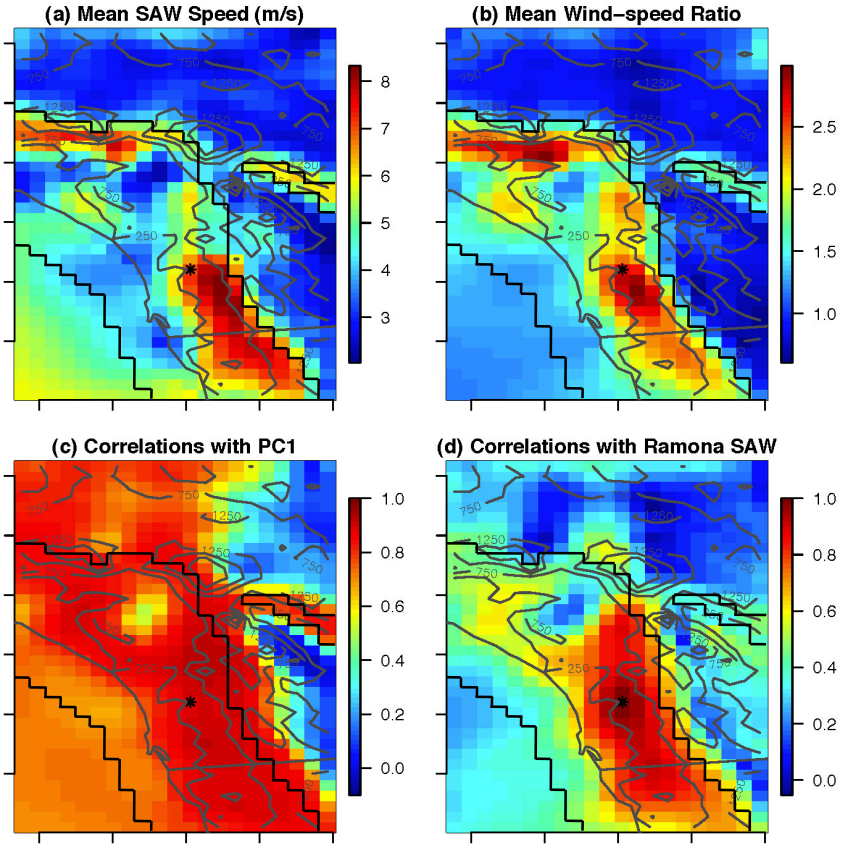

Figure 1.6. SAW spatial patterns. (a) Means, (b) Ratios of SAW to all other winds, (c) Correlations of local SAW time series with the leading SAW principal component (PC1), and (d) Correlations of SAWRI time series with Ramona SAW. Black line marks SAW Domain on each map. All means and correlations are based on hourly data.

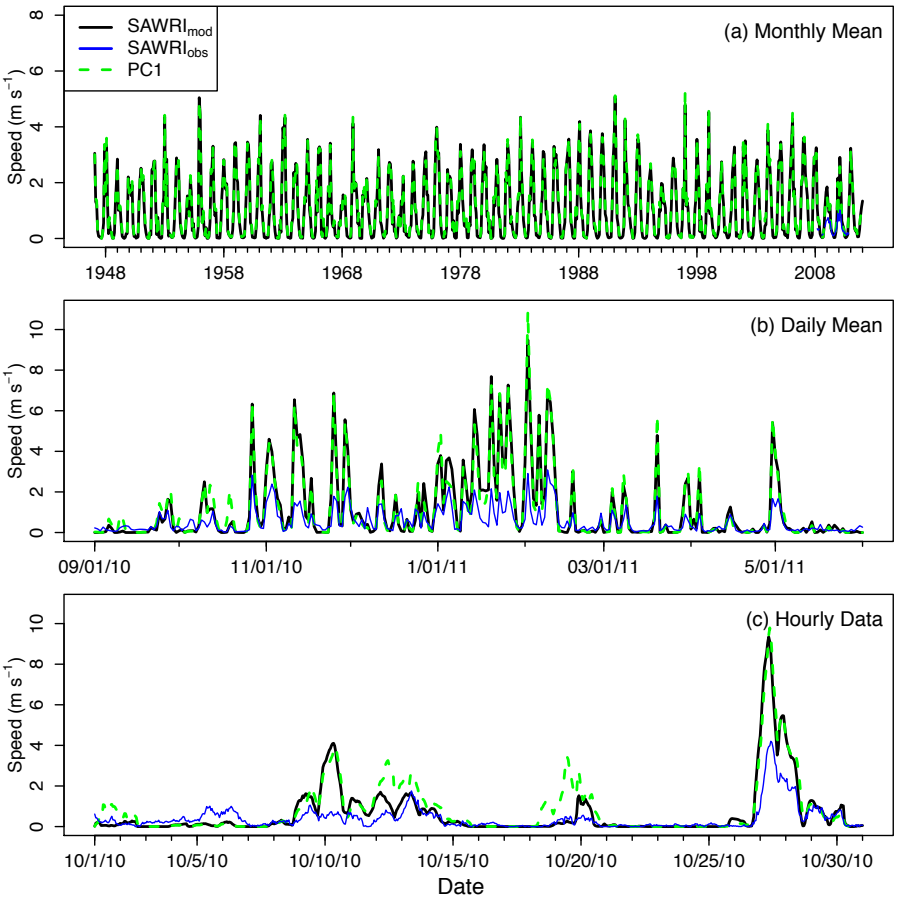

Figure 1.7. Comparison of SAWRI and SAWRI$_{obs}$ at different time scales. PC1 is shown (green) on each panel. (a) Monthly means over the CaRD10 record with two years (2009-2011) of available SAWRI$_{obs}$ (b) Daily means from Sep 2010 to May 2011, and (c) Hourly resolution time series for October 2010.

1.3 Results

1.3.1 SAW Climatology

Regionally, i.e., using SAWRI we detect a total of 2056 events on the 65-year record yielding an average of 32 occurrences per year. Typical SAW episodes last 1-2 days and represent 27% of the occurrences (Figure 1.8a). SAW events lasting up to 6 days account for 90% of all occurrences. The remaining 10% are made up almost entirely of events lasting between 7 and 12 days. Locally, the occurrence of events lasting 1-2 days is consistent with

regional detection (also 27% of all events). However, shorter events (between 12 and 24 hrs) are the most frequent (Figure 1.8b). This suggests that mild SAW pulses over most active SAW locations (red areas in Figure 1.6a) may not be detected regionally, as they dissipate before reaching the coast. The mean and maximum SAWRI representing events lasting up to 5 days appear to increase linearly with duration (Figure 1.8c,e). For events longer than 5 days, the mean and maximum SAWRI reach limit speeds (~5 and 9 m s^{-1}, respectively) regardless of their duration. The duration-intensity relation for local SAWs is comparable (see Figure 1.8d,f) to regional results.

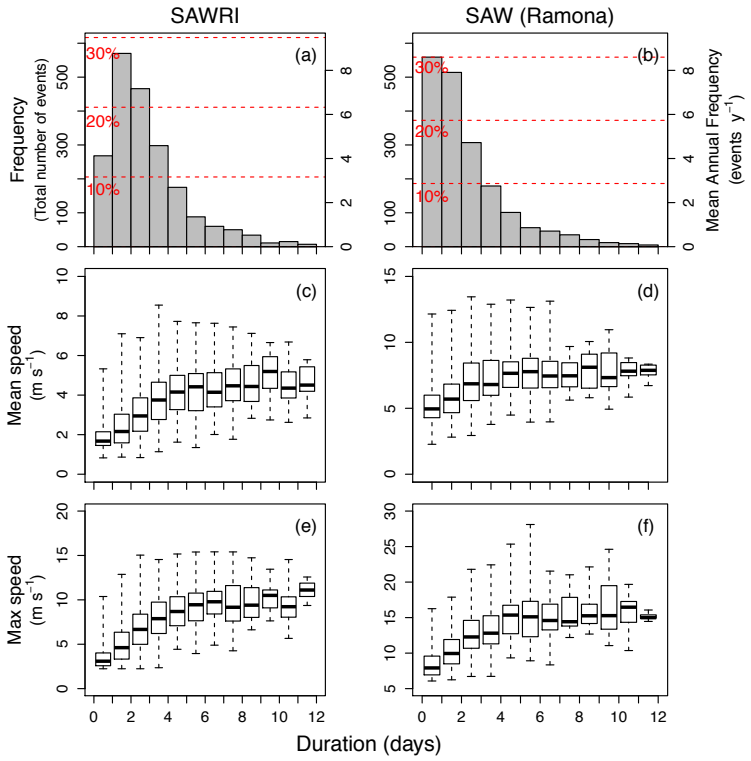

Figure 1.8. Events detected regionally (SAWRI) and locally (SAWs at Ramona)**.** Frequency (a, b) of total number of events in record (right axes) and mean number of events per year (left axes) separated by duration. Distribution of mean speed (c, d), and maximum speed (e, f) of events per duration bin. Bold lines show median values, boxes delimit the first and third quartiles, and whiskers mark maximum and minimum values for each group.

The SAW season extends from October to April, when SAW events occur at least twice per average month (Figure 1.9d). SAWs tend to be most frequent in December, but most durable and strong in January. Early and late season SAW episodes occur, on average, about once per month in September and May, and typically exhibit moderate duration, and moderate regional speeds, i.e., mean and maximum SAWRI (Figure 1.9a-c). Although not on our record, the two events of May 2014 (http://abcnews.go.com/topics/news/weather/santa-ana-winds.htm) appear to have been exceptional. This seasonal cycle of SAWs, although described in more detail here, generally agrees with seasonality identified in other studies (Raphael, 2003; Jones et al., 2010).

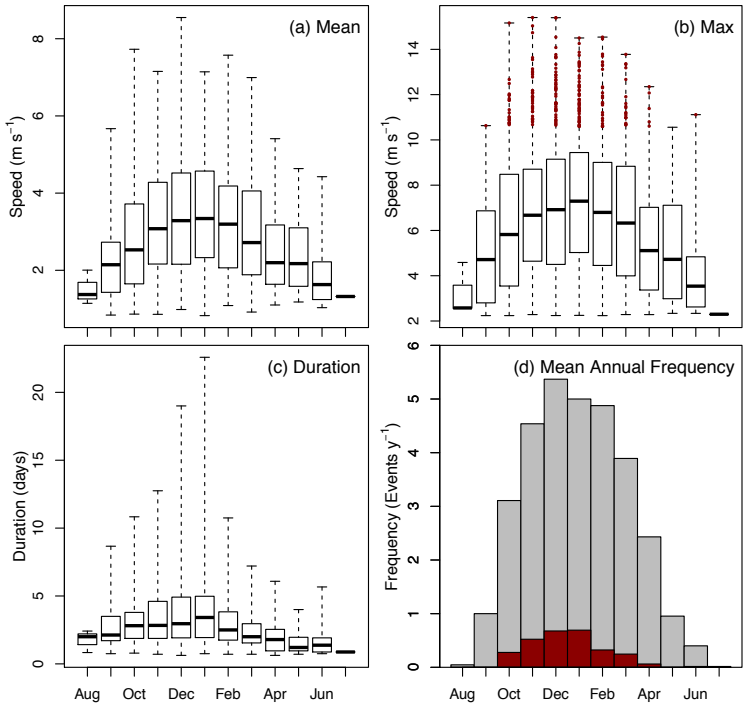

Figure 1.9. Climatology of regional SAW events (SAWRI). Monthly distribution of (a) mean SAWRI per event, (b) maximum SAWRI per event, (c) duration and (d) mean monthly frequency per season of SAW events detected from 1948 to 2012. In panels (a), (b) and (c) bold lines show median values, boxes delimit the first and third quartiles, and whiskers mark maximum and minimum values for each month. Extremes SAWs are shown in dark red in panels (b) and (d).

In addition to the seasonal cycle, the hourly SAWRI resolves a well-defined diurnal cycle (Figure 1.10), reaching their maximum in the morning, and decay to their minimum in the late afternoon. Local diurnal cycle of SAWs is line with SAWRI; however, inland and coastal locations are slightly different. At the coast, the on-shore sea breeze may to some extent counteract SAWs starting in the morning and during some events the winds may reverse in the late afternoon.

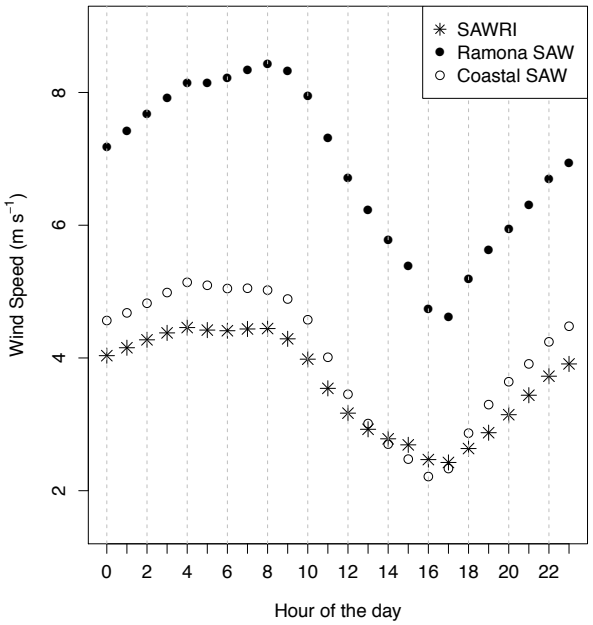

Figure 1.10. Regional (SAWRI), and local (Ramona and Coastal) diurnal cycles of SAWs. Wind speed average for each hour across all SAWs detected in record.

1.3.2 Climatology of SAW Extremes

Under the SAW and extreme definitions established, extremes account for 10% of the total number of events (on average 3 events per year). Extreme SAWs are most common in

December, and January, but also occur in the shoulder seasons, with more extremes in fall compared to spring (red histogram in Figure 1.9d). Even though the highest frequency of extreme events is observed during the coldest months, maximum SAWRI can be just as extreme in the fall (Figure 1.9b). For example, 3 out of the top 5 SAW events with maximum SAWRI above 15 m s^{-1} occurred in fall.

1.3.3 Variability and trends

Our results indicate considerable variability of SAW frequency, duration and total intensity (total or by category) on interannual to decadal time scales. There are no significant long-term trends (Figure 1.11a-c), except for a modest upward trend in the intensity of extreme SAWs (Figure 1.11d). For the record the frequency of extreme events account for 9% of all SAW events, but they contribute 25% to the total seasonal activity. Closer examination reveals that this trend results mainly from a step-function-type change that roughly corresponds to the North Pacific climate shift in the mid-1970s (Mantua & Hare, 2002). A similar shift is also evident in the SAW duration and activity (Figure 1.11b, c). The shift in these other variables, although not resulting in a significant trend, is much more in line with the 1976 PDO shift.

1.3.4 Potential seasonal predictability

The time series in Figure 1.11 indicate a change in the behavior of seasonal SAW intensities coinciding with the shift of the Pacific Decadal Oscillation (PDO) to its positive phase in 1977. This suggests that seasonal atmospheric anomalies associated with PDO teleconnections (Favre & Gershunov, 2009; Mantua & Hare, 2002) may influence SAW

activity. Because PDO teleconnections influence circulation anomalies via their modulation of El Niño-Southern Oscillation (ENSO) teleconnections (Gershunov et al., 1998), we examine total seasonal SAW intensity anomalies composited by ENSO and PDO phases. Moreover Raphael (2003) suggested a relationship between ENSO and late season (Feb-Mar) SAW frequency.

Intensity anomalies are shown in box-and-whisker plots spanning the composite samples and quantified in percent deviation from the 65-year SAWRI climatology (Figure 1.12). We use bootstrapping as in Gershunov et al. (1998) to test whether composite mean deviations from climatology are significant. We find a significant positive signal in El Niño/PDO(+) years amounting to ~10% increased intensity and a negative signal in La Niña/PDO(-) years amounting to ~10% decrease in regional SAW intensity. These are the same constructive ENSO/PDO interactions that account for predictable precipitation signals (Gershunov et al., 1998) such that enhanced/decreased SAW activity tends to coincide with enhanced/decreased precipitation seasonally. This bodes well for seasonal fire danger, but obviously there is a lot of scatter in the composites as is seen on Figure 1.12. The significant relationship we find between SAW and ENSO is broadly consistent with the suggestion of Raphael (2003) that El Niño is associated with longer SAW events, while contrary to (Berg et al., 2013) who suggest the opposite association. It is worth noting that the relationship we find between seasonal SAW intensity and ENSO appears to be partly modulated by PDO.

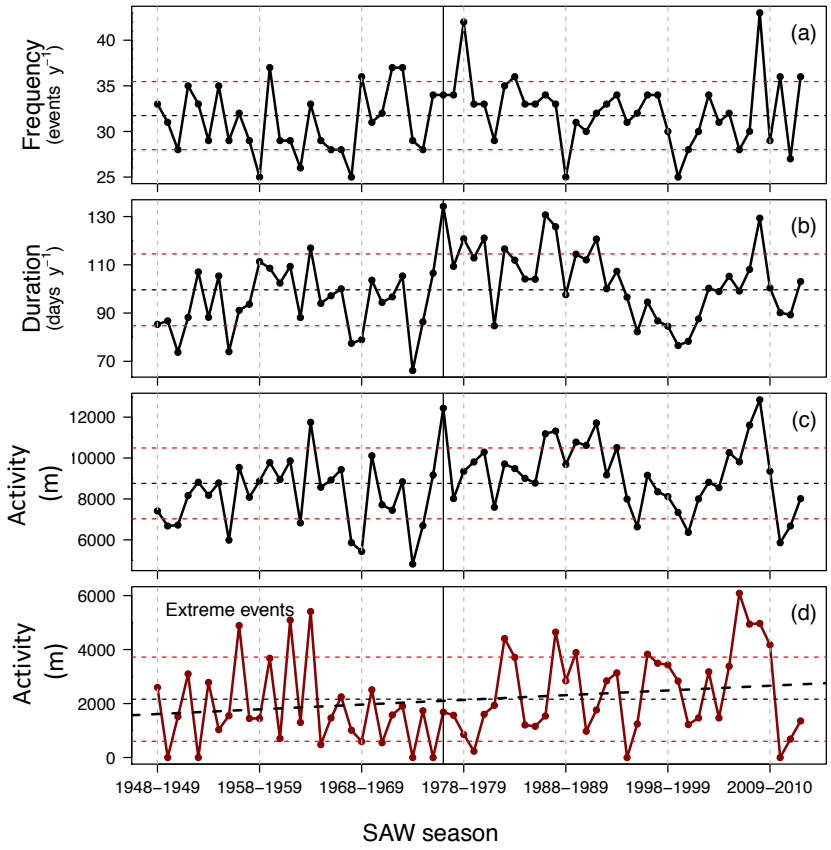

Figure 1.11. Seasonal (Aug-Jul) variability of total (a) Frequency, (c) Duration, (c) Activity and (d) Activity of extreme events. The linear regression fits are shown only if significant. Solid black line marks the change of PDO to its positive phase in 1976.

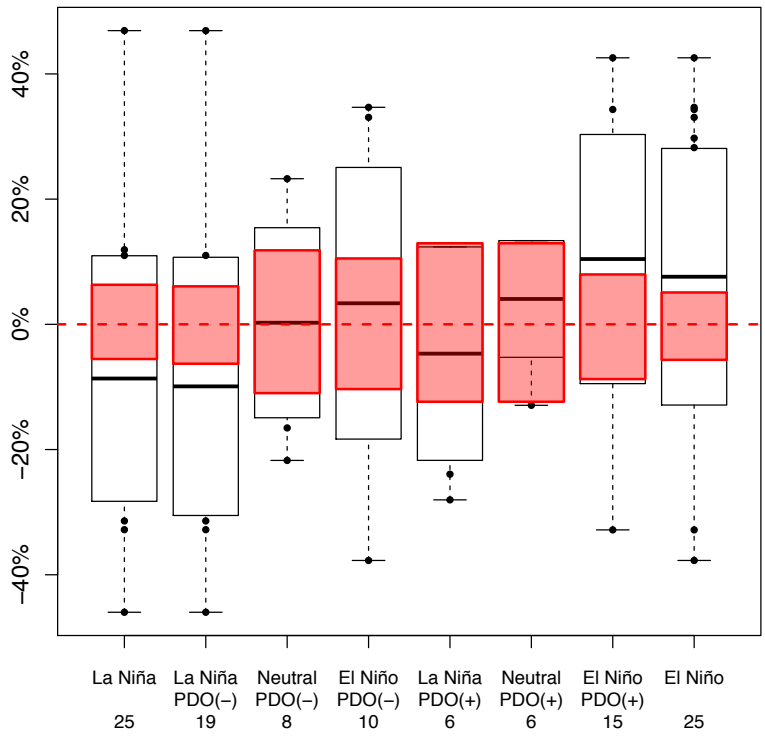

Figure 1.12. ENSO and ENSO-PDO joint composite anomaly of the integrated seasonal total SAWRI relative to the 65-year SAWRI climatology in percent. Numbers below each category are the number of SAW seasons (sample) that fell into the given composite. Boxes show one standard deviation from the mean, dots are outliers, and whisker marks the maximum and minimum outliers. Red boxes outline the 95% confidence region for means of bootstrapped (random) sampling distributions so that a sample mean lying outside the red zone signifies a statistically significant signal revealed with 95% confidence.

1.4 Discussion and conclusions

In this work, we present direct local and regional long-term perspectives on hourly Santa Ana winds that address specific voids in current knowledge: (1) constructing a long-term, high resolution, region-wide climatology against which the evolving SAW mean and extreme conditions in magnitude and time can be assessed, and (2) validation using a broad network of wind observations to realistically address local and regional variability.

The seasonal frequency of SAW clearly reflects mechanisms responsible for peak SAW frequency in December and January. These months have the least sunshine and longest nights essential for producing cold air masses over the Great Basin – the necessary condition for SAW. These months also experience a peak in transient synoptic activity that causes strong pressure gradients – the triggers of SAWs. On average longer events shift to higher SAWRI means and maxima up to 6 days but with a wide dispersion for each duration bin. The weak relationship between duration of SAW events and their maximum speeds agrees well with the fact that some events are mostly associated with local temperature gradient, while others are synoptically driven. A combination of these forcing mechanisms produces strong and long-lasting SAWs (Hughes & Hall, 2010). The cold air pooling over the elevated Great Basin also results in diurnal cycles of SAWs, which are strongest in the early morning hours when the thermodynamic mechanism is enhanced.

Under climate change, the Great Basin is projected to warm faster than the coastal region, which suggests that SAW occurrence may diminish (Hughes et al., 2011), However, the reconstructed historical record of SAWs does not thus far support such expectation. Instead, it raises new questions about future SAWs and fire seasons. The only long-term trend that we observe is in the extremes of SAWs, which appears to be related to the mid 70s North Pacific climate shift.

We find that seasonal SAW intensity is sensitive to prominent large-scale low-frequency modes of climate variability rooted in the tropical and North Pacific ocean-atmosphere system. These same modes are also known to predictably affect the hydroclimate of this region (Gershunov & Cayan, 2003). As is the case with regional seasonal precipitation anomalies, seasonal SAW intensity is enhanced during El Niño (especially if PDO is

positive) and subdued during La Niña (especially if PDO is negative) winters. This SAW intensification during El Niño/PDO(+) seasons may be due to the lower sea level pressure over the warmer coastal sea surface enhancing the off-shore pressure gradient that drives SAW. Our empirical results suggest that seasonal ENSO-related prediction of SAW activity and fire risk may be possible, a topic for further investigation. These results taken together with the known sensitivity of regional hydroclimate to global climate change(Polade et al., 2015) [*Polade et al.*, 2014], warrant a fresh look at climate change projections of SAWs, precipitation regime and fire risk.

Acknowledgment. This work was conducted thanks to the doctoral fellowship CONACYT-UCMEXUS (http://ucmexus.ucr.edu/) that provided financial support for Janin Guzman-Morales (scholar 214550). We also appreciate support from Climate Education Partners, an NSF funded project DUE-1239797 (www.sandiego.edu/climate). This study also contributes to DOI's Southwest Climate Science Center activities and NOAA's California and Nevada Applications Program award NA11OAR43101. The derived gridded data of local SAWs as well as the SAWRI can be accessed at http://cnap.ucsd.edu/data/janin/.

Chapter 1, in full, is a reprint of the material as it appears in *Geophysical Research Letters* in 2016, with slight modifications. Guzman-Morales, J., Gershunov, A., Theiss, J., Li, H., & Cayan, D. (2016). Santa Ana Winds of Southern California: Their climatology, extremes, and behavior spanning six and a half decades. *Geophysical Research Letters*, *43*(6), 2827–2834. https://doi.org/10.1002/2016GL067887 ©American Geophysical Union.

Used with permission. The dissertation author was the primary investigator and author of this paper.

APPENDIX 1

Reconstruction of SAWRI from Sustained Wind Observations

$SAWRI_{obs}$ is the average of RAWS winds over the SAW Domain (53 stations) during SAW periods. The selection of SAWs from the observations was done using the same method described in section 1.2.4. Data limitation allowed for two seasons (2009 and 2010) of $SAWRI_{obs}$ as observations were required in at least 70% of the stations to assemble $SAWRI_{obs}$, Although, better local skill is consistently achieved with observed gusts, we use sustained winds to define $SAWRI_{obs}$ because gusts, physically speaking, have local meaning only. The correlation between the hourly SAWRI and $SAWRI_{obs}$ is 0.6, and their consistency at different temporal resolutions is shown in Figure 1.7.

References

Abatzoglou, J. T., Barbero, R., & Nauslar, N. J. (2013). Diagnosing Santa Ana Winds in Southern California with Synoptic-Scale Analysis. Weather and Forecasting, 28(3), 704–710. https://doi.org/10.1175/WAF-D-13-00002.1

Berg, N., Hall, A., Capps, S. B., & Hughes, M. (2013). El Niño-Southern Oscillation impacts on winter winds over Southern California. Climate Dynamics, 40(1–2), 109–121. https://doi.org/10.1007/s00382-012-1461-

Boyle, T. C. (1995). The tortilla curtain. Viking.

Brasseur, O. (2001). Development and Application of a Physical Approach to Estimating Wind Gusts. Monthly Weather Review, 129(1), 5–25. https://doi.org/10.1175/15200493(2001)129<0005:DAAOAP>2.0.CO;2

Conil, S., & Hall, A. (2006). Local Regimes of Atmospheric Variability: A Case Study of Southern California. Journal of Climate, 19(17), 4308–4325. https://doi.org/10.1175/JCLI3837.1

Delfino, R. J., Brummel, S., Wu, J., Stern, H., Ostro, B., Lipsett, M., … Gillen, D. L. (2009). The relationship of respiratory and cardiovascular hospital admissions to the southern California wildfires of 2003. Occupational and Environmental Medicine, 66(3), 189–197. https://doi.org/10.1136/oem.2008.041376

Favre, A., & Gershunov, A. (2009). North Pacific cyclonic and anticyclonic transients in a global warming context: possible consequences for Western North American daily precipitation and temperature extremes. Climate Dynamics, 32(7–8), 969–987. https://doi.org/10.1007/s00382-008-0417-3

Fosberg, M. A. (1978). Weather in wildland fire management: the Fire Weather Index. U S For Serv Reprints of Articles by FS Employees. Retrieved from http://agris.fao.org/agris-search/search.do?recordID=US201302440660

Gershunov, A., Barnett, T. P., Gershunov, A., & Barnett, T. P. (1998). Interdecadal Modulation of ENSO Teleconnections. Bulletin of the American Meteorological Society, 79(12), 2715–2725. https://doi.org/10.1175/1520-0477(1998)079<2715:IMOET>2.0.CO;2

Gershunov, A., & Cayan, D. R. (2003). Heavy Daily Precipitation Frequency over the Contiguous United States: Sources of Climatic Variability and Seasonal Predictability. Journal of Climate, 16(16), 2752–2765. https://doi.org/10.1175/1520-0442(2003)016<2752:HDPFOT>2.0.CO;2

Gershunov, A., & Guirguis, K. (2012). California heat waves in the present and future. Geophysical Research Letters, 39(18). https://doi.org/10.1029/2012GL052979

Horel, J. D., & Dong, X. (2010). An Evaluation of the Distribution of Remote Automated Weather Stations (RAWS). Journal of Applied Meteorology and Climatology, 49(7), 1563–1578. https://doi.org/10.1175/2010JAMC2397.1

Hughes, M., & Hall, A. (2010). Local and synoptic mechanisms causing Southern California's Santa Ana winds. Climate Dynamics, 34(6), 847–857. https://doi.org/10.1007/s00382-009-0650-4

Hughes, M., Hall, A., & Kim, J. (2011). Human-induced changes in wind, temperature and relative humidity during Santa Ana events. Climatic Change, 109(S1), 119–132. https://doi.org/10.1007/s10584-011-0300-9

Jones, C., Fujioka, F., Carvalho, L. M. V., Jones, C., Fujioka, F., & Carvalho, L. M. V. (2010). Forecast Skill of Synoptic Conditions Associated with Santa Ana Winds in Southern California. Monthly Weather Review, 138(12), 4528–4541. https://doi.org/10.1175/2010MWR3406.1

Kalnay, E., Kanamitsu, M., Kistler, R., Collins, W., Deaven, D., Gandin, L., … Joseph, D. (1996). The NCEP/NCAR 40-Year Reanalysis Project. Bulletin of the American Meteorological Society, 77(3), 437–471. https://doi.org/10.1175/1520-0477(1996)077<0437:TNYRP>2.0.CO;2

Kanamaru, H., & Kanamitsu, M. (2007). Fifty-Seven-Year California Reanalysis Downscaling at 10 km (CaRD10). Part II: Comparison with North American Regional Reanalysis. Journal of Climate, 20(22), 5572–5592. https://doi.org/10.1175/2007JCLI1522.1

Kanamitsu, M., & Kanamaru, H. (2007). Fifty-Seven-Year California Reanalysis Downscaling at 10 km (CaRD10). Part I: System Detail and Validation with Observations. Journal of Climate, 20(22), 5553–5571. https://doi.org/10.1175/2007JCLI1482.1

Lu, W., Zhong, S., Charney, J. J., Bian, X., & Liu, S. (2012). WRF simulation over complex terrain during a southern California wildfire event. Journal of Geophysical Research: Atmospheres, 117(D5), n/a-n/a. https://doi.org/10.1029/2011JD017004

Mantua, N. J., & Hare, S. R. (2002). The Pacific Decadal Oscillation. Journal of Oceanography, 58(1), 35–44. https://doi.org/10.1023/A:1015820616384

Mesinger, F., DiMego, G., Kalnay, E., Mitchell, K., Shafran, P. C., Ebisuzaki, W., … Shi, W. (2006). North American Regional Reanalysis. Bulletin of the American Meteorological Society, 87(3), 343–360. https://doi.org/10.1175/BAMS-87-3-343

Moritz, M. A., Moody, T. J., Krawchuk, M. A., Hughes, M., & Hall, A. (2010). Spatial variation in extreme winds predicts large wildfire locations in chaparral ecosystems. Geophysical Research Letters, 37(4). https://doi.org/10.1029/2009GL041735

Polade, S. D., Pierce, D. W., Cayan, D. R., Gershunov, A., & Dettinger, M. D. (2014). The key role of dry days in changing regional climate and precipitation regimes. Scientific Reports, 4(1), 4364. https://doi.org/10.1038/srep04364

Raphael, M. N. (2003). The Santa Ana Winds of California. Earth Interactions, 7(8), 1–13. https://doi.org/10.1175/1087-3562(2003)007<0001:TSAWOC>2.0.CO;2

Sommers, W. T. (1978). LFM Forecast Variables Related to Santa Ana Wind Occurrences. Monthly Weather Review, 106(9), 1307–1316. https://doi.org/10.1175/1520-0493(1978)106<1307:LFVRTS>2.0.CO;2

Westerling, A. L., Cayan, D. R., Brown, T. J., Hall, B. L., & Riddle, L. G. (2004). Climate, Santa Ana Winds and autumn wildfires in southern California. Eos, Transactions American Geophysical Union, 85(31), 289. https://doi.org/10.1029/2004EO310001

Chapter 2

Downscaling of Winds in Southern California

2.1 Introduction

In Chapter 1, we have created and assessed the longest available record of Santa Ana Wind (SAW) activity spanning 1948 – 2012. This observationally validated dynamical record allowed us for the first time to robustly assess SAW variability on climate timescales. Although strong interannual and interdecadal modes of climate variability were for the first time elucidated for Santa Ana Wind activity, including extreme events, the record did not contain clear anthropogenic trends. However, we can expect changes in Santa Ana wind activity as the climate continues to warm non-uniformly over continents and oceans (e.g. Hughes et al., 2011). Therefore, we aim to assess any potential anthropogenic trends by application of our robust SAW detection methodology to highly frequency winds highly resolve in space. For this purpose, as well as for many potential other purposes (e.g. wind energy applications, public health impacts), we need to develop a capability to downscale daily wind fields from Global Circulation Models, which have resolutions roughly similar to the NCEP-NCAR Reanalysis 1 (R1), ~200X200 km for 10m winds.

Also, because wind observations are few and far between, an efficient and skillful statistical downscaling scheme would be very useful to update or extend the available dynamical records of winds without having to re-run the dynamical model, which is computationally expensive and not always possible. The methodology should in principle apply to dynamically downscaled winds at any spatial resolution.

The approach we choose, therefore, is to use our validated dynamical winds from CaRD10 (See Chapter 1) to train a statistical model for downscaling R1 winds onto the

CaRD10 grid. Such a statistical model, when properly optimized and validated on the observational period, could then be used to downscale winds from GCMs for the historical period and beyond into the projected future.

In this Chapter, we start by proposing and justifying a statistical approach to vector wind downscaling, apply it to R1 and CaRD10 data, and optimize it with respect to model complexity and skill. We then derive SAWs from downscaled daily wind fields and validate them with respect to the salient features of SAW climatology as reproduced by CaRD10 and assessed in Chapter 1. We authenticate the hybrid dynamical/statistical downscaling approach and thus lay the groundwork for its application to CMIP5 GCM simulations in Chapter 3.

2.2 Data and methods

2.2.1 Data Sets

For the development of the wind downscaling method, we use daily surface coarse resolution u- and v-wind fields from NCEP/NCAR Reanalysis 1 (R1, Kalnay et al., 1996) as well as daily average of fine resolution u- and v-wind fields from the California Reanalysis Downscaling at 10km (CaRD10, Kanamaru & Kanamitsu, 2007; Kanamitsu & Kanamaru, 2007) over an overlapping period of available data from 1948 to 2012. We employ six R1 grid cells (1.875˚ x 1.904˚) and 1764 CaRD10 grid cells (10 X 10 km) to cover an equivalent domain that extends 121˚W-116˚W in longitude and 36˚N-32˚N in latitude (Figure 2.1). This is a north-expanded version of the Cross Border Region (CBR) domain shown in Chapter 1 that now includes Ventura and Santa Barbara Counties. In what follows, we will refer to this Southern California domain as *SoCal*.

2.2.2 Canonical Correlation Analysis

We apply Canonical Correlation Analysis (CCA, Hotelling, 1935), a multivariate statistical technique, to identify spatial patterns in two fields of variables, whose temporal correlation is optimally correlated. We may refer to these as *canonical correlates*, *CCs*, or, alternatively, as *paired* or *coupled patterns*. In climate science, CCA has been used to diagnose coupled patterns (Roca & Gershunov, 2004) and associations between fields of variables (e.g. Guirguis et al., 2014; Schwartz et al., 2014) and in prognostic mode to predict meteorological variables or *predictands* from another set of large-scale climatic variables or *predictors* (Barnett & Preisendorfer, 1987; Gershunov & Cayan, 2003; Alfaro et al., 2006; García-Bustamante et al., 2012). In CCA prognostic application, the physical mechanism on which the predictive power relies is implicitly or empirically, rather than explicitly or theoretically accounted for by the statistical method itself, but the canonical correlates, on which the predictive model is based, elucidate the underlying physics of the climate system responsible for prediction skill (Gershunov & Cayan, 2003). In our approach, we use CCA to extract the statistical association between the finely resolved dynamically downscaled u- and v- winds from CaRD10 (predictand) and the coarsely resolved reanalysis u- and v-winds from R1 (predictor). The full description of the hybrid dynamical-statistical downscaling method is in section 2.2.3.

In this Chapter, we first assess the paired wind association patterns between R1 and CaRD10 by applying CCA in its diagnostic form. Following common practice, we reduced CaRD10 and R1 data dimensionality to p principal components (PC) from the Empirical

Orthogonal Functions (EOFs) of the u- and v-wind anomaly matrices. Data matrices for PCA, of both the coarsely and finely resolved wind fields, were constructed by concatenating daily u- and v-wind components corresponding to 65 years of available daily data (1948-2012).

We use the leading five PCs (p=5) summarizing 98% and 90% of the variance for the R1 and CaRD10 data, respectively. CCA input is not constrained to the same number of variables summarizing variability in the two fields; however, in this work we use the same number (p) for optimization of the statistical model (see section 2.2.3). CCA, then, computes linear combinations of the p PCs each summarizing the coarse and fine resolution wind fields to obtain k pairs of new variables called canonical correlates (CC)

$$\boldsymbol{CC_{k,x}} = \sum_{i=1}^{p} \boldsymbol{a_{k,i} x_i} \tag{2.1}$$

$$\boldsymbol{CC_{k,y}} = \sum_{i=1}^{p} \boldsymbol{b_{k,i} y_i} \tag{2.2}$$

where x_i and y_i are the i-th PCs of the u-/v-wind matrix from R1 and CaRD10 data, respectively; a and b are the linear combination coefficients; the maximum number of CC pairs is equal to the number of PCs fed to CCA (e.i., $k = p$). CC_k pairs refer to $CC_{k,R1}$ and $CC_{k,CaRD10}$, from now on, we simply refer to them as CC1, CC2 and so on when referring to the pair and add the data set subscript when distinction needs to be made.

2.2.3 Hybrid Dynamical-Statistical Downscaling

As mentioned previously, the downscaling method here developed is a hybrid approach based on the statistical association between dynamically downscaled winds

(CaRD10) and reanalysis winds (R1). Using CCA in its prognostic capacity, we relate daily coarse resolution winds from R1 with daily averages of fine resolution winds from CaRD10 (i.e., predictor/predictand) through k CCs derived from p PCs of each data set.

The statistical parameterization of the hybrid downscaling can utilize different combinations of p and k (where $k \leq p$). We compute downscaled wind fields using 15 p-k different configurations of increasing complexity resulting from allowing all possible k values for each p value up to p=5. We call the statistical downscaling or model from a particular p-k configuration as SD p-k.

For each SD p-k, we calculate cross-validated daily u- and v- winds, i.e, we trained the model on data from all years except the year to which the day to be predicted belongs. Thus, the cross-validation scheme requires to recalculate predictor and predictand PCs and associated CC pairs for every year of downscaled daily wind field (for our 1948-2012 record, it translates to 65 recalculations). This leave-one-out approach, similar to that used in Gershunov & Cayan (2003) provides a cross-validation of the model itself where the day to be predicted does not contribute to the statistical association from which is derived.

The skill of each statistical model is evaluated as the mean of the temporal correlations between the time series of R1 statistical downscaled u- and v-winds and CaRD10 u- and v-winds from all grid cell in the SoCal Domain.

2.2.4 Detection and Validation of Downscaled Santa Ana Winds

Definition and detection of R1-downscaled SAWs in the SoCal domain follow the method described in Chapter 1. In brief, the scheme for SAW detection is based on local direction and wind speed: SAWs are northeasterly filtered to wind speeds above the 75th

percentile of all northeasterly winds. This procedure is applied to each grid cell allowing spatial variability of SAW speed over the domain. The detection scheme's advantage in its application to statistically downscaled wind fields is that the wind speed error, relative to the training CaRD10 data, does not propagate to the selection of R1- or GCM-derived SAWs as speed thresholds are adjusted to each data set. In other words, this approach constitutes a GCM-specific wind speed bias correction in SAW detection.

2.3 Results

2.3.1 Coupled patterns of coarse and fine resolution winds fields and their relation with wind regimes in Southern California

The correlations between each pair of CCs are compiled in Table 2.1, and their time series for one season (Aug 2003 – Jul 2004) are illustrated in Figure 1.2. The temporal correlations of CCs with their corresponding gridded original data, this is $CC_{k,R1}$ - R1 and $CC_{k,CaRD10}$ - CaRD10, produce k=5 coupled spatial wind patterns of coarse and fine resolution, respectively (Figure 2.2). Thus, the proportion of the variance that each CC explains in the original wind data is given by the squared mean of the spatial correlation pattern ($\bar{r}^2$). The mean variability explained in u- and v-winds from both data sets (R1 and CaRD10) is summarized for each CC in Table 2.1.

The spatial patterns associated with the first three pairs of canonical correlates (CC1-CC3) and the original gridded data are equivalent in R1 and CaRD10, albeit obviously providing more spatial detail in the latter (Figure 2.2). For example, the two leading coupled modes (CC1 and CC2) together represent the onshore and offshore wind regimes, jointly providing control on the wind direction of these two main wintertime surface wind regimes

over SoCal, as described, for example, by Conil & Hall (2006). CC1 pair explains 65% of the zonal variability alone, whereas CC2 contains 51% of the meridional variability over the 10X10km grid (Table 2.1). Together, they explain 70% in each of the finely resolved (CaRD10) wind components over the SoCal domain. CC3 represents the upwelling-driving northerly alongshore wind peaking in the late spring and early summer (e.g. Conil & Hall, 2006), the wind that drives SoCal's regional coastal upwelling and low clouds (Clemesha et al., 2016; Macias et al., 2012). The CC3 pair is mostly correlated with northwesterly winds in its positive phase and accounts for at least 7% and 3% of the u- and v-wind CaRD10 variability.

The correlation patterns of CC4 and CC5 with CaRD10 and R1 winds are weak and not straightforward; neither are the spatial equivalents between the two data sets. $CC4_{CaRD10}$ shows the highest correlations with offshore winds over the southernmost region of the domain (San Diego-Tijuana) while $CC5_{CaRD10}$ correlates with winds along the coast in the southern part of the domain as well. We include these patterns (CC4 and CC5) here as they marginally improve the general downscaling skill for all winds, as we shall see below.

We would expect that a reconstruction of the wind field would require a bare minimum of the statistical association summarized by CC1-CC3 which accounts for ~75% of the total fine resolution wind variability. CC4 and CC5 pairs explain a small portion of the wind variance; however, their inclusion in the parametrization of the statistical downscaling improves the model correlation by up to 40% over the southwestern part of the SoCal domain (see section 2.3.2).

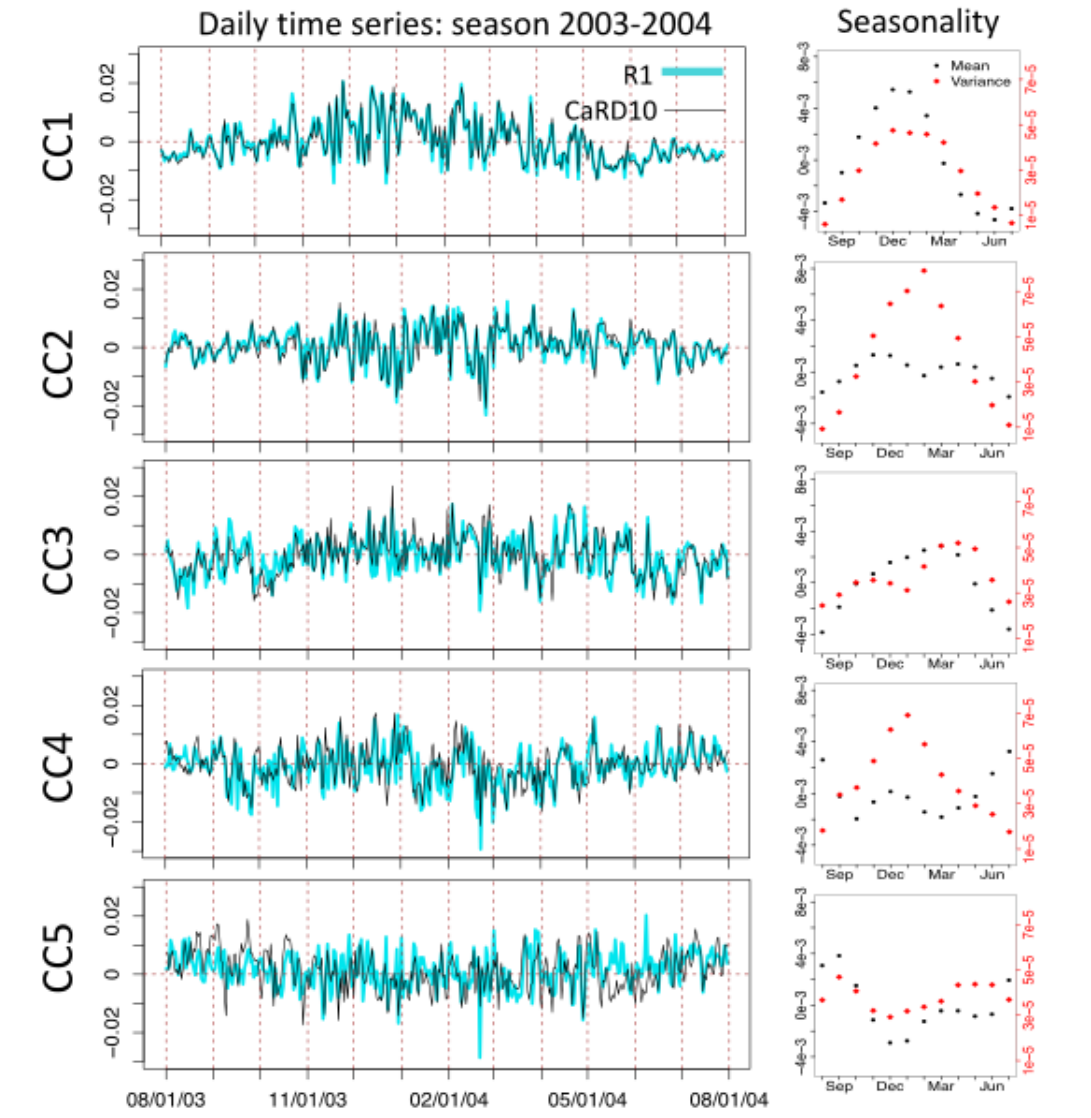

Figure 2.1. Canonical Correlates pairs. Rows correspond to the five CC pairs in increasing order (i.e., decreasing correlation between each other). Left column shows the time series of CC_{R1} (blue) and CC_{CaRD10} (black) for 2003-2004 season. Right column displays CC_{CaRD10} seasonality where black dots and red dots are the mean and variance values, respectively. Seasonality values are from 65 years (1948 to 2012).

Table 2.1. Mean explained variability by five canonical correlates in u- and v-winds of R1 and CaRD10 data sets.

		R1		CaRD10	
CC	**r**	**u-wind**	**v-wind**	**u -wind**	**v -wind**
CC1	0.94	87.6%	15.5%	65.0%	19.3%
CC2	0.91	2.8%	66.7%	4.7%	51.0%
CC3	0.76	2.8%	10.2%	4.4%	7.1%
CC4	0.65	4.0%	2.0%	7.6%	3.6%
CC5	0.48	0.9%	3.5%	3.7%	3.3%
Total	-----	**98.1%**	**97.9%**	**85.4%**	**84.3%**

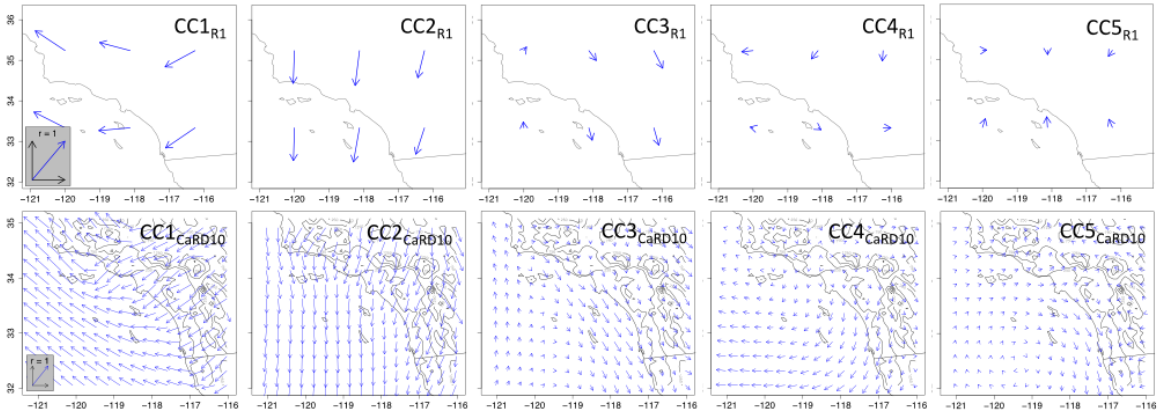

Figure 2.2. Correlation maps between CCs and original u- and v-wind data. Upper panels correspond to coarse resolution winds (R1) and lower panels to fine resolution winds (CaRD10). For clarity 60% of the data points were omitted in the depiction of CaRD10 correlation maps.

2.3.2 Skill of downscaled winds

The skill optimization surface (SOS) for u- and v-winds is shown in Figure 2.3. The highest skills are for the statistical models that use the maximum number of *k* for each *p* value, i.e., models with the same number of *p* PCs and *k* CCs located on the upper diagonal

of the SOS (SD 2-2, SD 3-3, SD 4-4, and SD 5-5). The simplest of those models, SD 2-2, yields a skill above 0.7 for both u- and v-winds which is in agreement with the first two CCs containing the largest portion of zonal and meridional winds variability. SD 5-5 produces the highest skill of about 0.8 also for both u- and v-winds; however, the skill improvement for *p=k* configurations between SD 3-3 and SD 5-5 is very low.

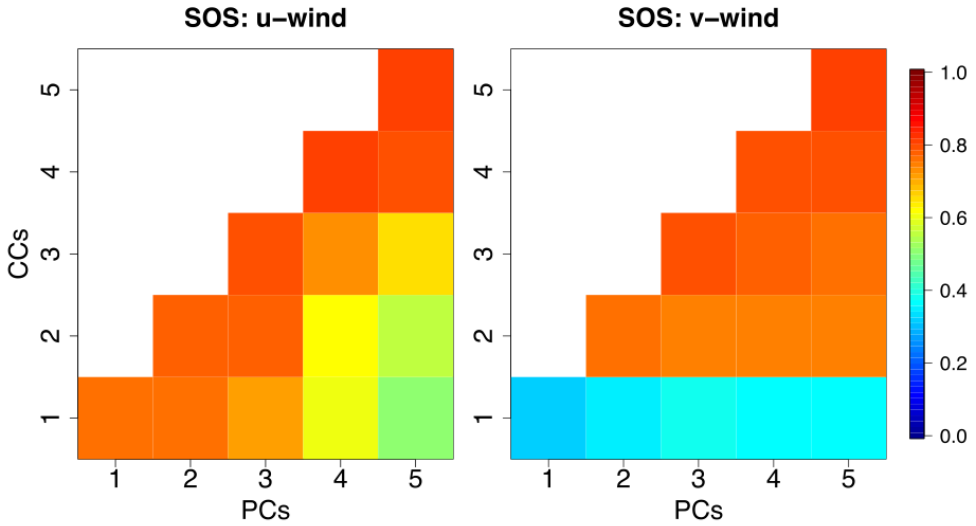

Figure 2.3. Skill Optimization Surface (SOS) of statistical downscaled 10-km resolution u- and v-winds. Skill for each *p-k* model complexity is the mean correlation from 1674 grid cells over the SoCal domain.

Closer examination of the correlations maps of models on the upper diagonal (from SD 2-2 through SD 5-5), shows that one-step addition of PC and CC produces very localized improvements. Figure 2.4 shows the various models' correlation map difference in percentage relative to the simplest skillful model SD 2-2. In u-wind maps, higher correlations are located in a topographically complex area entrenched between Santa Rosa Mtns and San Bernardino Mtns. Refinement of reproduced winds is also observed across San Rafael and

Santa Ynez Mtns and on the east side of San Bernardino Mnts. In the case of v-winds, progressively higher correlations result alongshore in line with CC3, CC4 and CC5 explaining mostly meridional wind variance in this region.

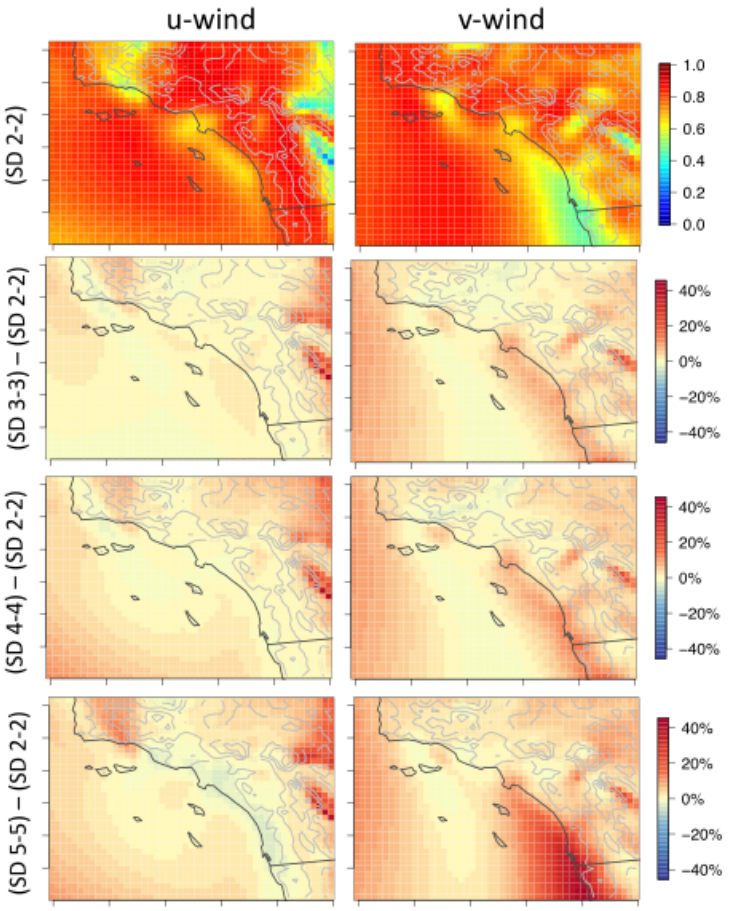

Figure 2.4. Correlation map of SD 2-2 with CaRD10 for u and v-winds (top two panels). Differences in percentage between SD of increasing complexity ($3 < p \geq 5$ and $p=k$) and SD 2-2 (lower panels).

In terms of wind direction and speed, models from SD 2-2 to SD 5-5 overall reproduce the wind distribution (Figure 2.5a-d) with most frequent and strongest winds from the northwest quadrant. However, winds roses showing statistical downscaled wind errors of

direction and speed in percentage relative to CaRD10 winds the model of highest complexity (SD 5-5) achieves the smallest wind direction and speed errors relative to CaRD10 winds (Figure 2.5e-h). Specifically, of all models in Figure 2.5, SD 5-5 provides the best winds distribution of wind direction and speed of less dominant northeasterly and southeasterly winds.

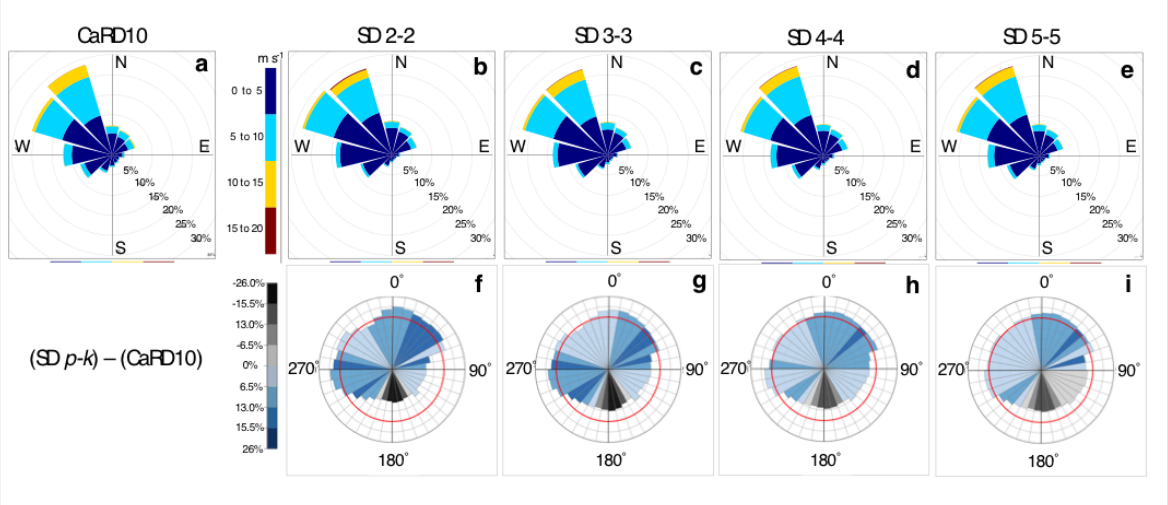

Figure 2.5. Wind roses of CaRD10 winds and downscaled winds with $2 < p \leq 5$ and $p = k$ (panels a-e) and corresponding errors of downscaled winds relative to CaRD10 data (panels f-i). Mean wind speed and frequency errors are calculated in 10˚ bins. Wind speed errors are shown in color scale and and frequency error are shown in radial scale. Red line equals to 0% error and every radial step is a 20% error. Therefore, bins falling inward and outwards the red line are under and over estimations, respectively.

2.3.2.1 Skill of the downscaled SAWs subset

Figure 2.6 shows the error wind roses of SAWs for the statistical models SD 2-2 to SD 5-5. Similarly to the error wind roses of all-winds, the sequential addition of PC-CC reduces both the wind distribution error and the wind speed error of downscaled SAWs. Therefore, the inclusion of canonical correlate pairs unrelated to the SAW regime (e.g., CC3 and CC5, both correlated with alongshore flow) provides more detail in the wind field

variability resulting in more realistic statistically downscaled winds. The statistical downscaling configuration SD 5-5 yields the smallest wind distribution error and wind speed error (+30% and -18%, respectively) relative to that observed in CaRD10 SAWs.

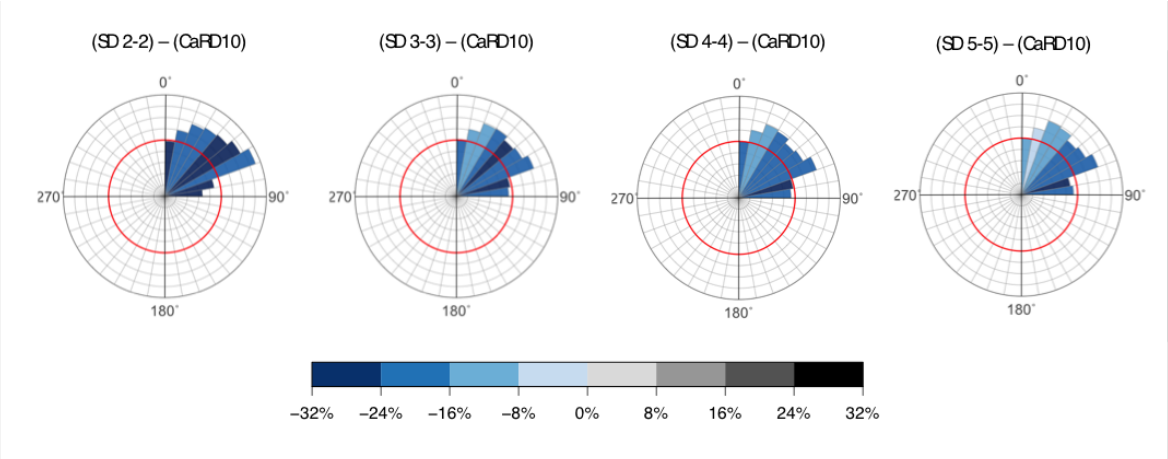

Figure 2.6. Wind roses of mean SAW speed and frequency errors in 10˚ bins. SAW speed errors are shown in color scale and SAW frequency error are shown by radial scale. Red line equals to 0% error and every radial step is a 20% error. Thus, bins falling inward and outwards the red line are under and over estimations, respectively.

As wind speed thresholds are fundamental to our locally detected SAWs, we revise the spatial distribution of downscaled SAW speed thresholds and compare to those from CaRD10. All SD fairly reproduce the wind speed threshold spatial fingerprint (Figure 2.7): stronger at the leeside of Laguna Mtn., San Gabriel Mtn., and across the coast of Ventura County. The most complex SD configuration (SD 5-5) yields the closest wind speed thresholds to CaRD10. The average of the wind speed thresholds over the SAW domain for SD 5-5 is 4.9 m s^{-1} (22.1% weaker than the corresponding value for CaRD10). Average errors for each SD configuration are shown in Figure 2.7.

Based on skill, wind direction error, and wind speed error for SAW detection, we deem SD 5-5 as the optimal statistical downscaling configuration. Thus, this configuration

was the one employed to downscale winds from GCMs and we referred to it as R1 SD in Chapter 3. Further validation of R1 SD is done in Chapter 3 and focuses on the parameters evaluated for describing the main features of SAWs.

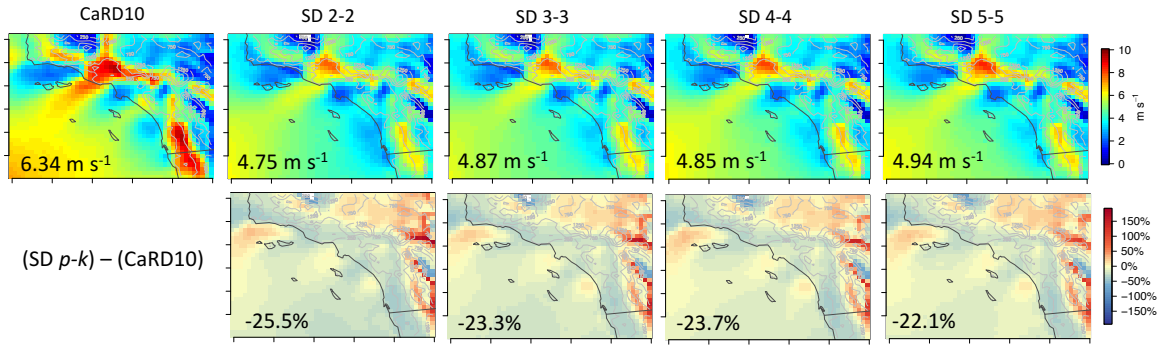

Figure 2.7. Maps of SAW speed thresholds for CaRD10 and statistical downscaling configurations from SD2-2 to SD 5-5 (upper panels). SAW speed threshold are defined as wind speed above the 75th percentile of all northeasterly winds detected at each grid cell. Errors of SAW speed thresholds relative to CaRD10 (lower panels). Mean speed thresholds and errors over the SAW domain are shown at the left-bottom corner of each map.

2.4 Summary, conclusions and future work

We have developed, performed and tested a hybrid dynamical/statistical approach to downscale daily wind vectors from a global reanalysis resolved on a coarse grid ~200X200 km onto a fine 10X10 km grid covering SoCal. The prognostic statistical downscaling model based on CCA applied to a dynamically produced training data set (u and v daily 10km winds from CaRD10), evaluated for physical meaning, optimized and evaluated for skill. In Chapter 3 of this dissertation, we apply the statistical method so achieved to downscale daily wind fields over SoCal from eight CMIP5 GCMs. The resulting daily 10X10 km gridded surface wind fields covering a period from 1950 to 2100 over the SoCal domain will be made

publicly available. We expect these data to contribute to research motivated by various applications from energy to public health.

After thus downscaling all daily R1 winds, we applied the Santa Ana Wind detection methodology of Guzman Morales et al. (2016) to obtain daily SAWs from R1 (1948-2017) and validated them with respect to various metrics representing SAW activity over SoCal. The hybrid dynamical/statistical downscaling methodology performed well in terms of the salient features of SAWs including realistically rendered seasonal cycle, interannual variability, and historical extreme events.

Our statistical approach can be applied to other dynamically downscaled wind products, including those at finer resolutions. This should allow for flexibility and skill in extending short dynamical wind data sets over longer historical periods as well as beyond to the GCM-projected futures. Our unique methodology will be applied in Chapter 3 to downscale CMIP5 historical simulations (1950-2005) and future climate projections.

Chapters 2 in full, has been submitted for publication to *Geophysical Research Letters*, with slight modifications. Guzman-Morales, J., and Gershunov, A. (2018). Climate Change Suppresses the Santa Ana Winds of Southern California and Sharpens their Seasonality. *Submitted for publication in GRL*. The dissertation author was the primary investigator and author of this paper.

References

Alfaro, E. J., Gershunov, A., & Cayan, D. (2006). Prediction of Summer Maximum and Minimum Temperature over the Central and Western United States: The Roles of Soil Moisture and Sea Surface Temperature. *Journal of Climate*, *19*(8), 1407–1421. https://doi.org/10.1175/JCLI3665.1

Barnett, T. P., & Preisendorfer, R. (1987). Origins and Levels of Monthly and Seasonal Forecast Skill for United States Surface Air Temperatures Determined by Canonical Correlation Analysis. *Monthly Weather Review*, *115*(9), 1825–1850. https://doi.org/10.1175/1520-0493(1987)115<1825:OALOMA>2.0.CO;2

Clemesha, R. E. S., Gershunov, A., Iacobellis, S. F., Williams, A. P., & Cayan, D. R. (2016). The northward march of summer low cloudiness along the California coast. *Geophysical Research Letters*, *43*(3), 1287–1295. https://doi.org/10.1002/2015GL067081

Conil, S., & Hall, A. (2006). Local Regimes of Atmospheric Variability: A Case Study of Southern California. *Journal of Climate*, *19*(17), 4308–4325. https://doi.org/10.1175/JCLI3837.1

García-Bustamante, E., González-Rouco, J. F., Navarro, J., Xoplaki, E., Jiménez, P. A., & Montávez, J. P. (2012). North Atlantic atmospheric circulation and surface wind in the Northeast of the Iberian Peninsula: uncertainty and long term downscaled variability. *Climate Dynamics*, *38*(1–2), 141–160. https://doi.org/10.1007/s00382-010-0969-x

Gershunov, A., & Cayan, D. R. (2003). Heavy Daily Precipitation Frequency over the Contiguous United States: Sources of Climatic Variability and Seasonal Predictability. *Journal of Climate*, *16*(16), 2752–2765. https://doi.org/10.1175/1520-0442(2003)016<2752:HDPFOT>2.0.CO;2

Guirguis, K., Gershunov, A., Tardy, A., & Basu, R. (2014). The Impact of Recent Heat Waves on Human Health in California. *Journal of Applied Meteorology and Climatology*, *53*(1), 3–19. https://doi.org/10.1175/JAMC-D-13-0130.1

Guzman-Morales, J., Gershunov, A., Theiss, J., Li, H., & Cayan, D. (2016). Santa Ana Winds of Southern California: Their climatology, extremes, and behavior spanning six and a half decades. *Geophysical Research Letters*, *43*(6), 2827–2834. https://doi.org/10.1002/2016GL067887

Hotelling, H. (1935). The most predictable criterion. *Journal of Educational Psychology*, *26*(2), 139–142. https://doi.org/10.1037/h0058165

Hughes, M., Hall, A., & Kim, J. (2011). Human-induced changes in wind, temperature and relative humidity during Santa Ana events. *Climatic Change*, *109*(S1), 119–132. https://doi.org/10.1007/s10584-011-0300-9

Kalnay, E., Kanamitsu, M., Kistler, R., Collins, W., Deaven, D., Gandin, L., … Joseph, D. (1996). The NCEP/NCAR 40-Year Reanalysis Project. *Bulletin of the American Meteorological Society*, *77*(3), 437–471. https://doi.org/10.1175/1520-0477(1996)077<0437:TNYRP>2.0.CO;2

Kanamaru, H., & Kanamitsu, M. (2007). Fifty-Seven-Year California Reanalysis Downscaling at 10 km (CaRD10). Part II: Comparison with North American Regional Reanalysis. *Journal of Climate*, *20*(22), 5572–5592. https://doi.org/10.1175/2007JCLI1522.1
Kanamitsu, M., & Kanamaru, H. (2007). Fifty-Seven-Year California Reanalysis Downscaling at 10 km (CaRD10). Part I: System Detail and Validation with Observations. *Journal of Climate*, *20*(22), 5553–5571. https://doi.org/10.1175/2007JCLI1482.1

Macias, D., Landry, M. R., Gershunov, A., Miller, A. J., & Franks, P. J. S. (2012). Climatic Control of Upwelling Variability along the Western North-American Coast. *PLoS ONE*, *7*(1), e30436. https://doi.org/10.1371/journal.pone.0030436

Roca, R., & Gershunov, A. (2004). Coupling of latent heat flux and the greenhouse effect by large-scale tropical/subtropical dynamics diagnosed in a set of observations and model simulations. *Climate Dynamics*, *22*(2–3), 205–222. https://doi.org/10.1007/s00382-003-0376-7

Schwartz, R. E., Gershunov, A., Iacobellis, S. F., & Cayan, D. R. (2014). North American west coast summer low cloudiness: Broadscale variability associated with sea surface temperature. *Geophysical Research Letters*, *41*(9), 3307–3314. https://doi.org/10.1002/2014GL059825

Chapter 3

Climate Change Suppresses the Santa Ana Winds of Southern California and Sharpens their Seasonality

We applied the statistical downscaling component developed in Chapter 2 to eight GCMs to downscale daily u and v surface wind vectors at 10x10km resolution. To these downscaled wind field, we subsequently applied the automated windspeed- and direction-based SAW detection approach to derive the Regional SAW Index (SAWRI) described in Chapter 1 (Guzman-Morales et al., 2016), and validated them further with respect to their abilities to simulate key features of the SAW climatology. Finally, we assessed the behavior of projected SAWs, paying special attention to changes in their extreme occurrences, during the first and last halves of 21st Century. We found SAW activity decrese in the shoulders of the season and smallest decreases in Novermber-December-January near the peak of the season. The decreases are mainly driven by changes in frequency and less so by changes in intensity. These changes are observed in the two projection periods of the 21st century under examination but intensify by the last half of century. The modest decrease in the most frequent and stronger SAWs in winter altogether with independent projections of diminishing precipitation in the fall would result in a shift of the traditional peak of the wildfire season (October) to later months. Nonetheless, less desicatting SAWs during fall, the effect of increasing precipitation year-to-year variability to the availability of dry vegetation fuel, as well as land–human dynamics are factors yet to be quantified.

3.1 Introduction

Coastal California's wildfire season displays a unique seasonality. While the rest of western North America and much of the vegetated world are susceptible to wildfires during summer, coastal California's fire season peaks, historically, in the fall. This timing is determined by a climatic coincidence of two seasonal factors: the dry and gusty downslope winds, whose season starts in the fall when vegetation is at its seasonal driest after the long dry calm summer and before the first rains of winter defining this Mediterranean climate regime. The downslope wind systems desiccating California's coastal ranges, although probably synoptically related, are regionally distinct. Among these are the Diablo Winds of Northern California's Bay Area, the Sundowners of Santa Barbara and Ventura Counties, and the Santa Ana winds of Southern California (SoCal, a domain that in our reckoning includes the border region with Northern Baja California). The Santa Ana Winds (SAWs) are dynamically distinct from the rest and probably the most notorious for fanning California's largest wildfires. When vegetation is dry, the fires fanned by these winds are largely uncontrollable. SAW-fanned wildfires typically rage in the sloping coastal backcountry, with its encroaching wildland-urban-interface (WUI), where the gusty downslope SAWs are the strongest (Guzman-Morales et al., 2016) and ignitions are nearly always human-caused (Syphard & Keeley, 2015). While the local impacts of these wildfires are devastating (https://www.nytimes.com/2017/12/05/us/california-wildfire-ventura.html, https://www.newyorker.com/culture/cultural-comment/after-the-mudslides-an-absence-in-montecito), the smoke blowing towards the densely populated coastal zone exposes much larger and diverse populations to remote respiratory health impacts (Delfino et al., 2009). Smoke impacts can, moreover, be exacerbated by out of season coastal heat waves driven by

the SAWs themselves adiabatically, via compression of air descending to sea level (Kalkstein et al., 2018).

The largest wildfire in California's recorded history, the Thomas Fire, was recently fanned by Santa Ana winds and raged through most of December 2017 into January 2018, when the first significant rains of the water year occurred. Beyond the duration and magnitude of this fire, its most unusual feature was its December timing. Following a bone dry fall and early winter, the vegetation was desiccated in December 2017, allowing successive SAWs to fan the Thomas Fire. Although SAW activity peaks in December (Guzman-Morales et al., 2016), the vegetation is typically no longer flammable by then as several rain storms would have normally occurred by that late into the wet season. However, climate change is projected to decrease the frequency of precipitation in California (Polade et al., 2015, 2017), particularly in SoCal and especially in the shoulder seasons of fall and spring (Pierce et al., 2013). This is expected to result increasingly more often in dry flammable fuels persisting into the peak of the SAW season, which is during the traditional wet season, and therefore in a lengthening wildfire season (Jennings et al., 2018). This reasoning is predicated on the assumption of no significant change in future SAW activity. In this work, we examine the validity of this assumption.

Guzman-Morales et al., (2016, hereafter GM'16) developed a historical 65-year catalog of hourly SAWs, validated them with the available observations, analyzed their climatology and variability at different time scales, and identified potential sources of seasonal predictability. GM'16 detected SAWs purely from wind speed and direction. Although significant multidecadal variability was observed, this longest available record of SAWs did not manifest trends attributable to anthropogenic causes.

Two studies directly addressed changes of SAWs in future climate projections. These studies provided conflicting results. First, Miller & Schlegel (2006) assessed projected climatological monthly changes of SAW occurrences as detected using large scale pressure gradient in two Climate Model Intercomparison Project, Phase 3 (CMIP3, Meehl et al., 2007) global climate models (GCMs) forced by low (B1) and high (A2) IPCC4 emission scenarios. Their results suggested a decline of SAW occurrences in September but a significant increase in December, at the peak of the SAW season, in the last 30 years of the 21st century relative to the equivalent period of the 20th century. However, variation in those results was identified in the early and middle parts of the 21st century between models and emission scenarios. The second study by Hughes et al. (2011) used one dynamically downscaled CMIP3-generation GCM under A1B scenario to generate a local gap-flow-based projection of SAWs. This study reported an all-season (Oct-Mar) mean decrease of ~20% in the number of annual Santa Ana days by mid 21st century from which only Oct and Feb had a statistically significant decrease. This anthropogenic change was attributed to the disproportionate warming of the cold pool of air over the Great Basin relative to that of the coastal marine airmass, attenuating the temperature gradient between the Great Basin and the Pacific Ocean off the coast of California, which is an important thermodynamic mechanism for the formation of SAWs (Hughes & Hall, 2010).

Two related studies, Yue et al. (2014) and Jin et al. (2015) addressed the SoCal wildfire regime change and explicitly estimated SAWs as climatic drivers for mid-21st century projections of total SoCal burned area. Their results show increases of 40% and 64%, respectively, of total burned areas over a comparable region. Resolving the historical fire season, Sep – Nov, and using seven CMIP3 GCMs and an approach similar to Miller &

Schlegel (2006) to project SAWs for the mid-21st century in a middle-of-the-road A1B scenario, Yue et al. (2014) report an increase of wildfire activity in November associated with an increase of SAWs during that month. However, model agreement is weak and the overall increase of wildfires seems to respond mainly to projected general future warming and drying than to an increase in SAW activity. Jin et al. (2015) using five GCMs from CMIP5 (Taylor et al., 2012) forced by RCP8.5 and a dynamical downscaling approach as well as a local SAW definition similar to Hughes et al., (2011), attribute the increase in their mid-21st century projected Santa Ana (SA) wildfire category also mostly to the reduction of relative humidity and to a lesser extent to increasing wind speed during SAW events. The inconsistencies in projected SAW trends over the 21th century identified by the above-mentioned studies seem to arise, at least partially, from differences in the approach used to define, detect and downscale SAWs as well as from the limited choice of GCMs in some studies. In our work we construct future projections of SAWs based on a hybrid (dynamical-statistical) downscaling of daily winds (u and v vectors on a 10X10km grid) over the SoCal domain in a set of eight GCMs. These GCMs were previously validated for their general climate realism over this region and we validate them further with respect to their ability to reproduce key features of SAW (Section 3.3.2). Using these downscaled GCMs, we provide a description of future SAW behavior focusing on changes in SAW activity, reflecting changes in frequency, intensity, and seasonality, as well as on extreme SAW events (Section 3.3.3). We then examine the synoptic cause of projected SAW trends - the pressure gradient force (Section 3.3), and conclude by discussing the results in the context of SoCal's changing wildfire regime (Section 4).

3.2 Data and Methods

3.2.1 Downscaling of winds from GCMs

For the downscaling of winds fields from GCMs, we retrieve daily historical (1950-2005) u- and v- surface wind fields from eight Global Climate Models (GCMs) as well as their future projections (2006-2100) forced with the "business as usual" RCP8.5 emissions scenario (IPCC 2013). These 8 GCMs (Table 3.1) were those providing the requisite daily data among the ten GCMs previously selected, from a total of 31 CMIP5 GCMs, for their realism in reproducing several key features of the California climate (California Department of Water Resources, Climate Change Technical Advisory Group, Lynn et al., 2015). We utilize equivalent domains to that used for the development of our hybrid dynamical/statistical downscaling presented in Chapter 2, a region extending 121˚W-116˚W in longitude and 36˚N-32˚N in latitude.

The optimal statistical downscaling configuration described and evaluated in Chapter 2 was then applied to the eight GCM simulations from 1950 to 2100.

3.2.2 GCM-derived SAWs selection and validation

For each GCM, daily SAWs were detected at each 10X10km grid cell in the resultant downscaled SoCal domain following our SAW local detection scheme (Chapter 2). Subsequently, the Santa Ana Wind Regional Index (SAWRI) was derived. Physically, SAWRI is the daily mean SAW speed computed over the grid cells within the SAW domain and therefore is expressed in speed units (m s^{-1}).

We assessed the GCMs' ability to reproduce SAWRI by quantifying its behavior, e.g. frequency, intensity, seasonality, timing, and sensitivity to its synoptic driver - the pressure

gradient force (PGF) - over the historical period by comparison to SAWRI derived from R1D and CaRD10 winds. Table 3.1 summarizes these validation results for the eight GCMs, which are discussed in Section 3.3.2. The validation helps us to interpret anthropogenic trends in projected SAW activity. Unless otherwise stated, *SAW Activity* is defined as the accumulation of SAWRI over the relevant period in question (e.g. month, year). We focus on projected changes occurring in two time periods: the first and second halves of the 21st Century, 2000-2049 and 2050-2099, respectively. Changes are evaluated relative to the last half of the 20th Century, 1950-1999.

3.2.3 Quantifying SAW sensitivity to Synoptic Pressure Gradient Force (PGF)

To validate GCMs with respect to their ability to realistically reproduce the salient synoptic-scale patterns of Sea Level Pressure associated with SAWs, we use SLP data from R1 and GCMs in a synoptic domain that expands from (227.5˚E, 50˚N) to (255˚E, 25˚N) in its most northeast and southwest points, respectively. GCM's future projections (RCP8.5) of SLP were also used to track changes in synoptic patterns. SLP climatology from 1950 to 2005 was subtracted in all data sets before subsequent computations.

We computed daily SLP anomalies in the synoptic domain for R1 and GCM data sets during the historical validation period shared by R1 and the GCMs (1950-2005). Associated Pressure Gradient Force (PGF) fields were derived as the negative of the SLP gradient in the x and y direction:

$$PGF_{xy} = PGF_x + PGF_y = -\sqrt{\frac{\Delta p^2}{\Delta x} + \frac{\Delta p^2}{\Delta y}} \tag{3.1}$$

m Then, for each data set (R1 and GCMs) we produce a map of correlations evaluated in the x-y (lon-lat) space between the corresponding SAWRI and the PGF resolved over the synoptic domain:

$$r_{PGFxy,SAWRI} = \sqrt{r_{PGFx,SAWRI}{}^2 + r_{PFGy,SAWRI}{}^2} \quad (3.2)$$

The sub-region where $r_{PGFxy,SAWRI}$ values are above the 95th percentile of correlations across the synoptic domain is continuous and coincides well with the SAW region, and defines the region of maximum PGF-SAW association in all data sets (Figure 3.1). The spatial mean correlation in this region is 0.71 in the R1 data set, and ranges from 0.65 to 0.92 in GCMs. Daily average PGF over this SAW-relevant sub-region (PGF_{r95}) was retrieved for every SAW day in the historical validation period. We then linearly regressed SAWRI and PFG_{r95}.

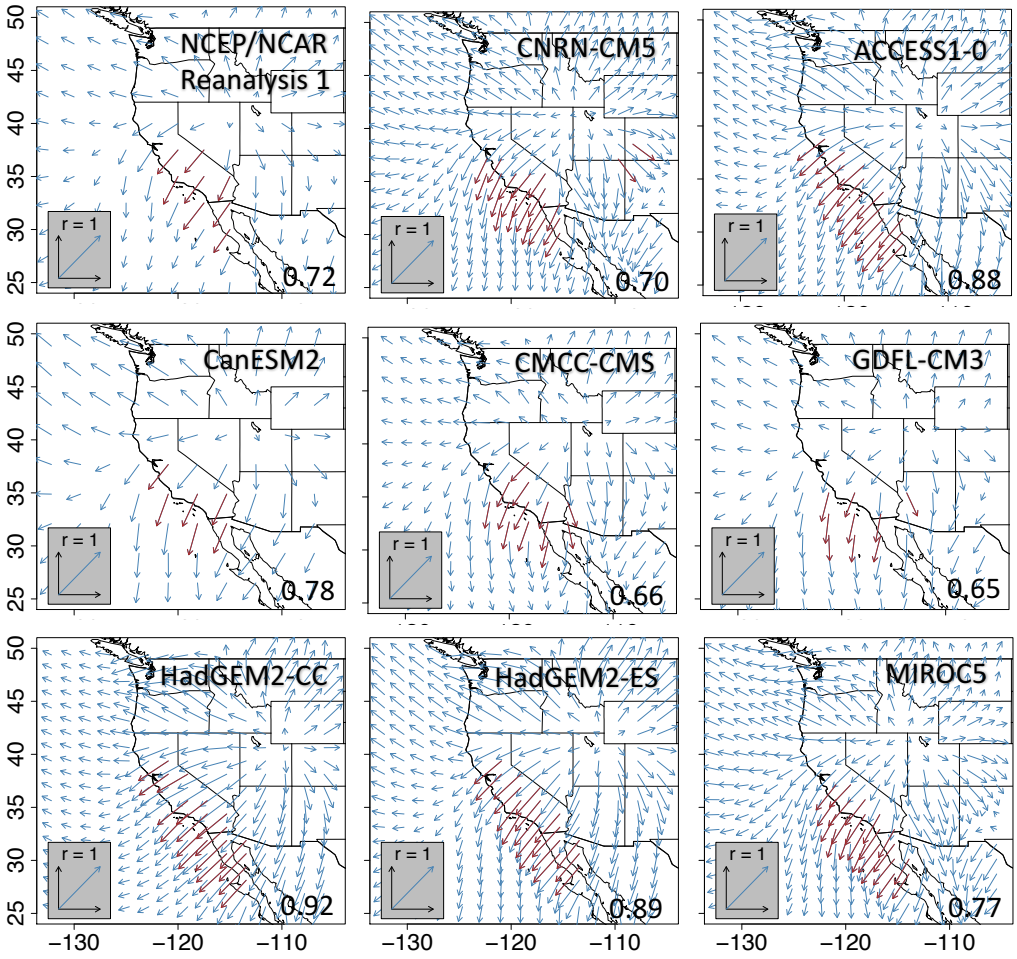

Figure 3.1. PGF and SAWRI correlation ($r_{PGFxy,SAWRI}$) maps. Correlations above the 95th percentile are shown in brown arrows and their mean values $\left(\bar{r}_{95th}\right)$ are at the left bottom corner for each map.

3.3 Results

3.3.1 SAW Sensitivity to Synoptic Pressure Patterns

The SLP composite of SAW days from R1 shows a high anomaly located over the east side of the Great Basin centered at the intersection of Nevada, Utah and Idaho (Figure 3.2a), traditionally considered the signature large-scale SLP forcing of SAWs (Abatzoglou et al., 2013; Raphael, 2003; Sommers, 1978). This SLP anomaly creates a northeasterly PGF

field over a region that covers most of California, expanding from the San Francisco Bay Area to Northern Baja California. The average PGF_{r95} (highlighted in red arrows on Figure 3.2) during all SAW days amounts to 91 Pa m^{-1}. Deriving downslope SAWs from large circulation, i.e. PGF, would require consideration of topography, vertical katabatic acceleration and friction terms; here instead, we intend to develop a quantitative relationship between a metric derived from large-scale SLP anomaly patterns and regionally-averaged SAWs based on simplified synoptic-scale forcing considerations – circulation features that may be affected by climate change.

All eight models reasonably reproduce a realistic SLP composite anomaly pattern and associated northeasterly PGF field over the relevant regional domain, i.e. California and Northern Baja California (Figure 1) during SAW days. The composite SLP anomaly shape variation between GCMs seems responsible for the variations in PGF directions over the area of high correlations (r_{95}). Despite these differences, the mean PGF_{r95} associated with the SLP anomaly in GCMs is comparable (77.1 Pa m^{-1} – 95.2 Pa m^{-1}) to that manifest in R1 (91 Pa m^{-1}).

The pressure gradient force (PGF_{r95}) explains 68% (r=0.83) of the daily variability of SAWRI in the R1 data set and between 40% and 67% ($0.63 < r < 0.82$) in GCMs. The linear fit between SAWRI and PGF_{r95} is shown in Figure 3.3 and the associated correlation coefficients and slopes are summarized in Table 3.1. The quantitative evaluation of SAWRI sensitivity to PGF in GCMs relative to R1 is further discussed in section 3.3.2, whereas the SAWRI versus PGF_{r95} changes in the 21st Century are addressed in section 3.3.3.

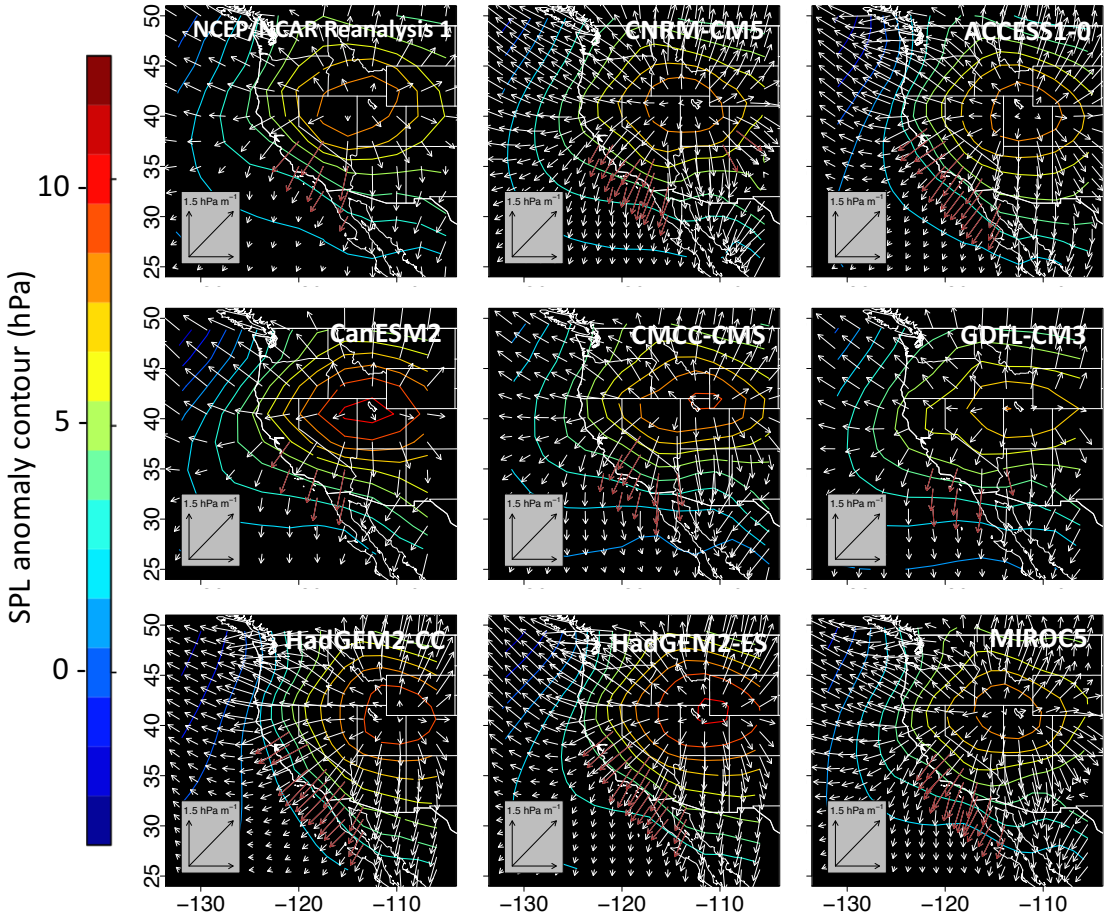

Figure 3.2. SLP and PGF composite maps during SAW days. SLP anomalies are shown by contour lines and associated PFG field is indicated by white arrows. Brown arrows mark the region where correlation between PGF and SAWRI is above the 95th percentile as shown in Figure 3.1.

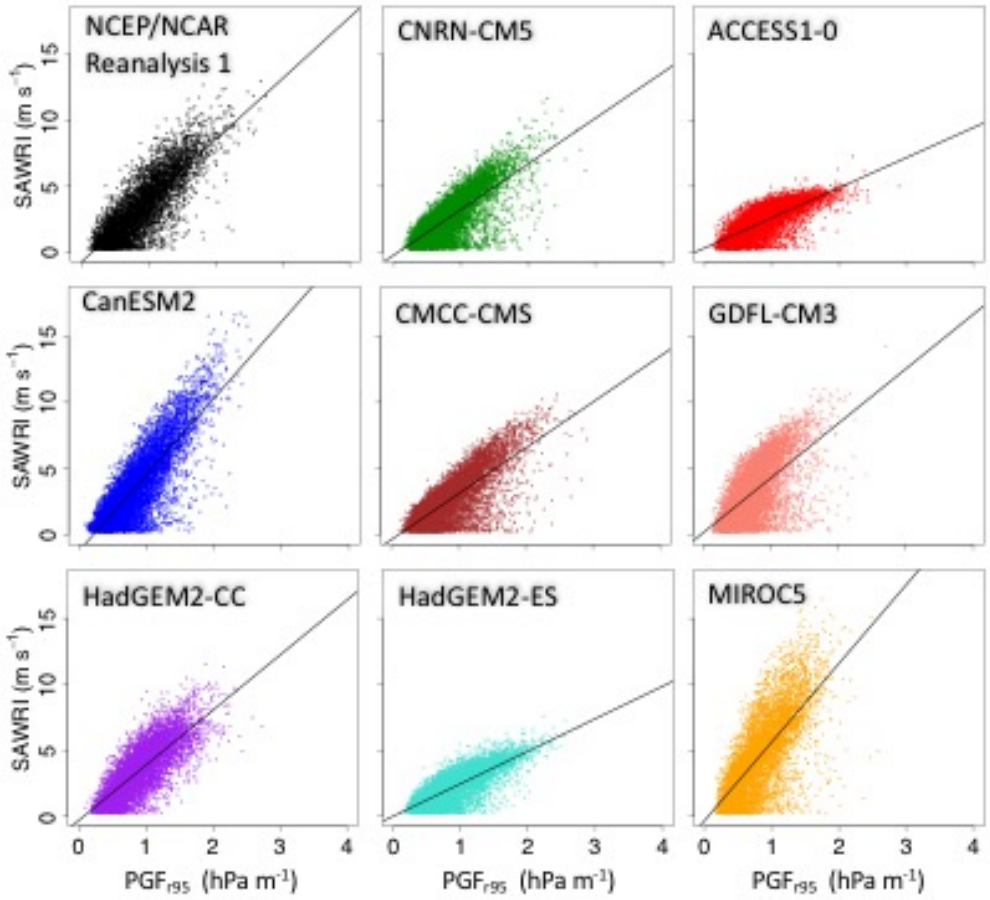

Figure 3.3. SAWRI sensitivity to PGF_{r95} of all R1 and GCMs. Plots are from daily values when SAW conditions are present (SAWRI>0) in the historical validation period (1950-2005). Black lines show the linear fit whose slope and correlation coefficient are listed in Table 3.1.

3.3.2 GCMs' Downscaled Performance in Reproducing SAWs

No GCM can be considered "best" for realistically capturing all SAW features evaluated here. With respect to total seasonal SAW activity, CNRM-CM5, CMCC-CSM, ACCESS1-0, and HadGEM2-ES have negative bias relative to R1, whereas CanESM2, GDFLCM-3, HadGEM2-CC, and MIROC5 yield larger positive bias (Figure 3.4a, Table 1.3). A closer examination of SAW frequency and intensity (as summarized by SAWRI),

which together define total seasonal SAW activity, allows us to identify the source of bias in seasonal SAW activity for each GCM. All models overestimate the frequency of SAW days but vary on the sign of intensity error (Figure 3.4b, Table 1.3). CNRM-CM5 and CMCC-CSM overestimate frequency and underestimate intensity by a similar degree yielding the closest mean total annual SAW activity and associated inter-annual variability compared to R1. ACCESS1-0 and HadGEM2-ES show larger underestimations of SAWRI (-32% in both cases), corresponding to a larger negative bias in total annual SAW activity. By contrast, the positive bias of SAW activity from GDFL-CM3 and HadGEM2-CC is dominated by the overestimation of SAW frequency, while intensity errors are remarkably small. Finally, CanESM2 and MIROC display the least realistic performance with the highest overestimations of SAW frequency and intensity, respectively, that produces the largest positive errors in annual SAW activity.

GCMs generally reproduce SAW seasonality: monthly SAW activity ramping up through fall, peaking in winter, and gradually declining by late spring (Figure 3.4c). All GCMs manifest no or negligible SAW activity over summer, JJA. ACCESS1-0, and HadGEM2-ES show the most realistic seasonality with the smallest monthly SAW activity difference relative to R1D (21 and 18.5 m s^{-1}, respectively), measure as the root sum of squared differences across all months in the SAW year (Aug-Jul). By breaking down seasonal total SAW activity, again into frequency and intensity, we observe that the amplitude differences in seasonality are dominated by intensity errors (Figure 3.5a-b), while deviation in shape is better explained by frequency errors (Figure 3.5c-d) as is the case for the overestimation of SAW activity in fall for CMCC-CMS and GDFL-CM3. According to R1D, the annual maximum SAW day tends to occur on Dec 31 ±29 (1 standard deviation)

days (Figure 3.4d). CNRM-CM5, and MIROC5 yield the closest timing falling within two days of what is recorded historically, but displaying a larger spread.

Table 3.1. Summary of GCMs' performance in reproducing SAW features: activity, frequency, intensity, seasonality, timing of annual maximum SAW day, and sensitivity to PGF. Differences, and errors in the table are relative to R1 SD (first row), and are mean values of 56 years in the historical validation period (1950-2005). SAW activity differences in seasonality between GCMs and R1 SD are measured as the root sum of squared differences of all moths in the SAW year (Aug-Jul), and the sign retained in parenthesis indicate the direction of models' bias. The two smallest values for each metric are marked with asterisks.

Data Set	Activity (m)	Frequency (y^{-1})	Intensity ($m\ s^{-1}$)	Seasonality (m)	Timing of annual maximum SAW day	Sensitivity to PGF	
						Slope $m_{PFG-SAWRI}$	Correlation coefficient $r_{SAWRI-PGF}$
R1 SD	316.4	89.5	3.47	----------	Dec 31	4.6	0.83
CNRM-CM5	-9.9 (-3.1%)*	+17.4 (+19%)	-0.66 (-19%)	(-) 24.3	-0.1*	-1.2	0.75
ACCESS1-0	-45.7 (-14.6%)	+22.5 (+25%)	-1.10 (-32%)	(-) 21.0*	+9.6	-2.4	0.74
CanESM2	+134.1 (+43.0%)	+26.5 (+30%)	+0.40 (+11%)	(+) 57.0	-22.1	+1.1	0.82*
CMCC-CMS	-11.1 (-3.5%)*	+13.9 (+16%)*	-0.56 (-16%)	(-) 34.2	-12.4	-1.2	0.76
GDFL-CM3	+36.7 (+11.7%)	+14.1 (+15%)*	-0.11 (-3%)*	(+) 48.4	-14.3	-0.5*	0.63
HadGEM2-CC	+80.7 (+25.8%)	+20.3 (+22%)	+0.10 (+3%)*	(+) 51.7	+6.9	-0.5*	0.78*
HadGEM2-ES	-47.0 (-15.1%)	+22.1 (+25%)	-1.10 (-32%)	(-) 18.5*	+10.3	-2.2	0.78*
MIROC5	+184.5 (+59.1%)	+15.9 (+17%)	+1.22 (+35%)	(+) 80.04	-2.1*	+1.3	0.71

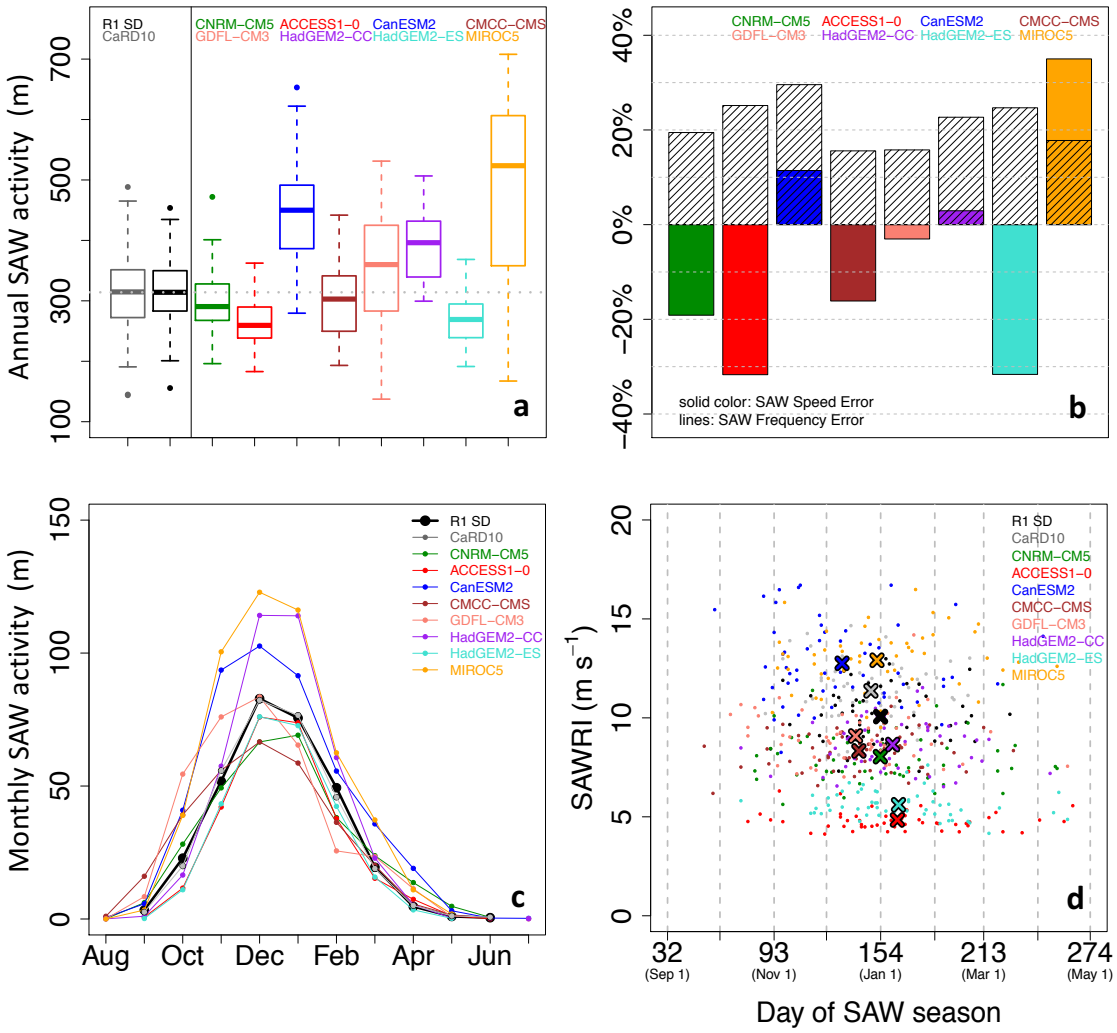

Figure 3.4. Validation of SAWs derived from downscaled GCMs. All values are seasonal means for 56 seasons in the historical validation period (1950 -2005), unless stated otherwise. CaRD10 is included here for comparison purposes (grey). Panel (a): Annual (Aug-Jul) SAW activity. SAW activity is the sum of SAWRI over the SAW year (Aug-Jul). Thick lines within boxes show the median. Lower and upper box limits correspond to the 25th and 75th percentiles, respectively. Whiskers extend to the most extreme data point which is no more than 1.5 times the inter-percentile range from the box. Grey dashed horizontal line marks the R1D SAWRI median across all models. Panel (b): Frequency and speed errors. Panel (c): Seasonality of SAW activity (sum of SAWRI over each month) Panel (d): Timing of strongest SAW day**.** Timing is recorded as the day number at each SAW season (Aug 1-Jul 31). Dots represent each season.

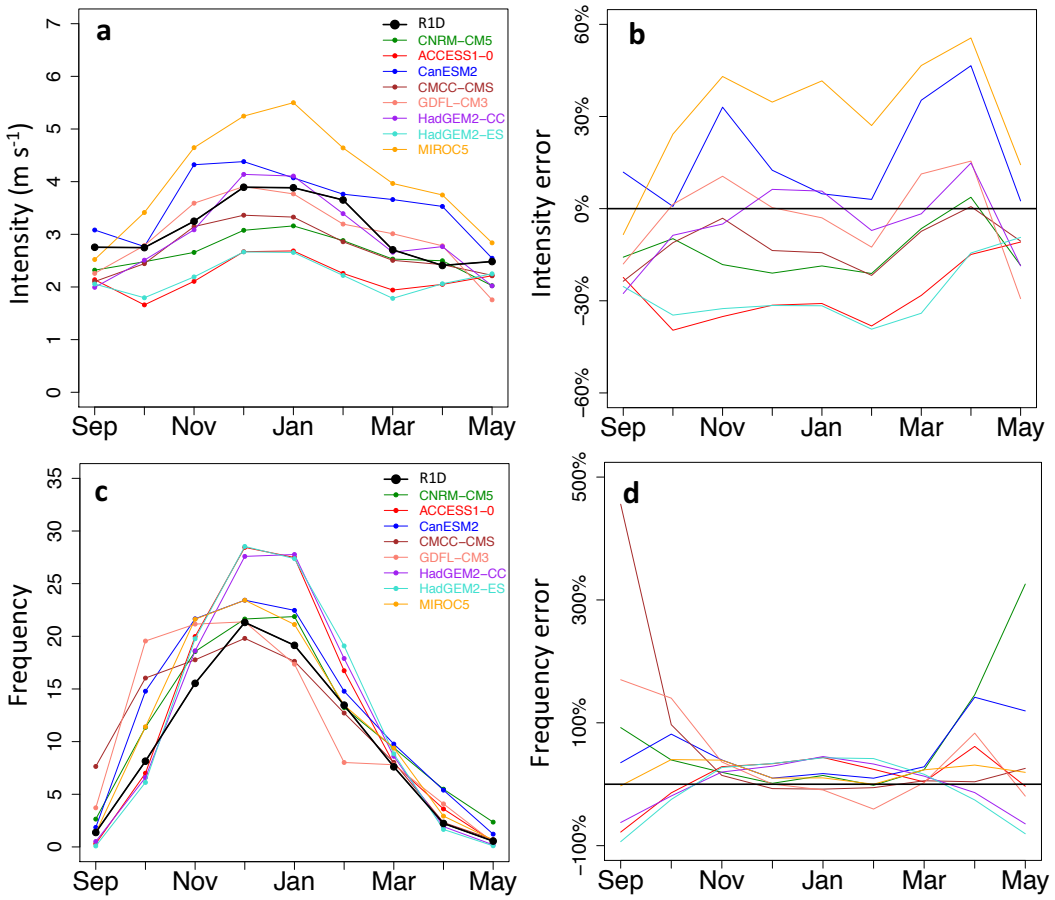

Figure 3.5. Seasonality of SAW Frequency and Intensity. Errors are relative to R1 SD seasonality. All values represent mean values from 56 seasons in the historical validation period (1950-2005).

In terms of SAWRI sensitivity to daily variations in PGF, HadGEM2-CC, HadGEM2-ES, and CanESM2 display the highest and most realistic correlations, with the PGF explaining between 60% and 67% of the daily SAWRI variance. Differences in the linear fit slope (Table 3.1) show that HadGEM2-CC and GDFL-CM3 detect the most realistic magnitude of SAWRI response to PGF_{r95} variability, while HadGEM2-ES and ACCESS1-0 underestimate the most the effect of PGF variations on SAWRI (flattest slopes).

In summary, there are no clear winners or losers among the models. Therefore, it is difficult to highlight a subset of these 8 GCMs when we consider projected changes in Santa Ana winds. Results of these validation exercises, however, will help interpret elements of projected SAW changes by illuminating individual model idiosyncrasies.

3.3.3 Projections of SAWs through the 21st Century

All GCMs project a decrease of total seasonal SAW activity during the first half of the 21st century (not shown) that intensifies during the last half century. The reduction of SAW activity is -18.5% ±4.5% on seasonal average. Meanwhile, the decrease of extreme SAW activity (the 10% of the strongest events) is about twice as large (-34.3% ±9.2%) as shown in Figure 3a. The reduction of SAW activity is explained by a larger reduction in SAW frequency than in intensity, according to most models (Figure 3.6). This is especially true for extremes SAWs, where the reduction in intensity is very small (-0.81% ±0.99%) relative to the reduction in frequency (-33.8% ±9.9%).

In terms of seasonality, reduction of SAW activity is robust across all months and all GCMs (Figure 3.6c) with very few exceptions: CNRM-CM5, CMCC-CMS, HadGEM2-CC, and GDFL-CM3 show an increase of SAW activity in Oct (+14%), Nov (+11%), Sep (+273%), and Feb (+45%), respectively. However, the actual SAW activity detected by HadGEM2-CC in Sep is unrealistically weak, while SAW activity detected by GDFL-CM3 in Feb is considerably smaller than that in the R1D historical record (Figure 3.4c).

In the second half of the 21st century on average, Nov and Dec are projected to have the smallest decrease of SAW activity of about -12% on average. At the tails of the SAW season, the average reduction reaches -68% (Sep) and -50% (May) with a higher decrease

over the early season (Sep-Oct) than over late season (Mar-May). For extreme SAWs, we find a more pronounced decrease overall with similar proportional distribution across the season, that is, smallest decreases around the peak season in Nov and Dec (-25%) with greater decreases early and late in the season (Figure 3.6c). Our results are in general agreement with those of Hughes et al. (2011) who show the stronger decrease at the shoulder of their season (Oct and Feb) and a slight, nonetheless not statistically significant, increase at the second most active month of the season (Jan).

We find no agreement among GCMs regarding changes in the mean timing of annual maximum SAW day (Figure 3.6d). GCMs do not show consistent changes towards a specific time of the season or consistent tendency within-model for the first and last half of the 21st century. It is noteworthy, however; that the strength of maximum annual SAW day shows a very modest average decrease (2.1–8.4%) consistent with smaller intensity reductions projected for extreme SAW winds as compared with average SAWs.

Lastly for all GCMs, except CanESM2, we find that the decrease in SAWRI is associated with a decrease of PGF_{r95} regardless of the specific SAWRI-PGF_{r95} sensitivity (Figure 3.7). SAW-associated PGF is not projected to clearly decrease in that model, while SAWs slightly decreases regardless. The other GCMs show a remarkable consistency in the cause of projected decrease in SAW activity as well as in its evolving trend through the 21st century.

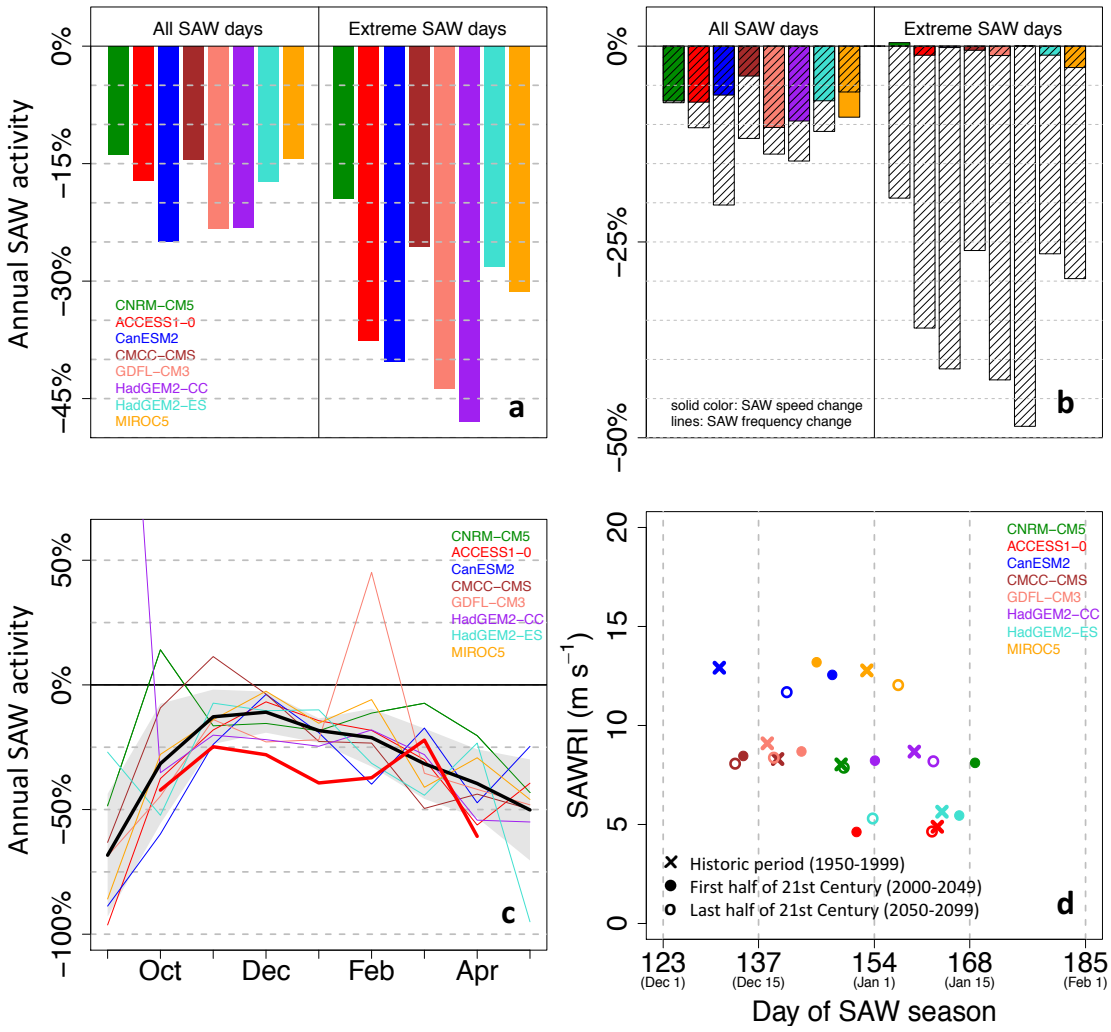

Figure 3.6. Future projection of SAWs features. Changes are for the last half of the 21st Century (2045-2099) and are relative to the the base historical period (1950-1999). Panel (a): Percentage change of total seasonal SAW run for all SAW days (left) and extreme SAW days (right). Panel (b): Percentage change of wind speed and frequency for all SAW days (left) and extremes SAW days (right). Panel (c): Percentage change of the SAW run seasonality. Thick black line shows the all GCMs mean and grey envelopes ± 1 standard deviation. Thick red line corresponds to the all GCMs mean change of extreme SAWs. Panel (d): Timing of maximum annual SAW day. Changes for the first half of the 21st Century are also included in panel (d).

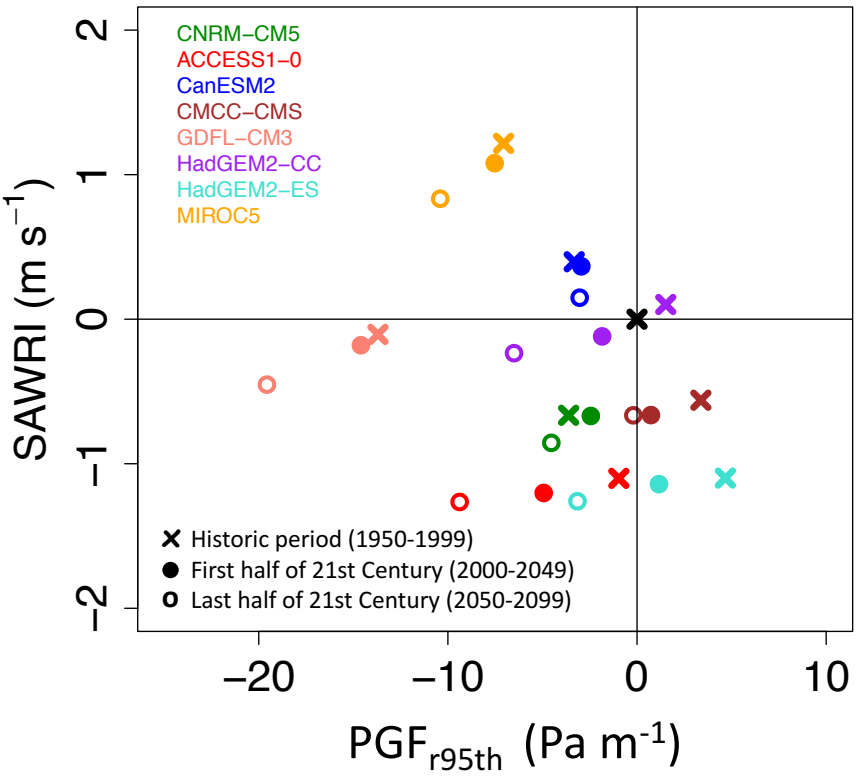

Figure 3.7. SAW sensitivity to changes in PGF. Values are mean from 50 years corresponding to the periods here examined. All values are referenced to R1D (black cross at 0,0).

3.4 Summary, discussion and conclusions

We have used a hybrid dynamical-statistical approach to downscale 10m winds from coarsely resolved winds in a 7-decade-long global Reanalysis (R1) and a set of eight GCMs forced with historical and future (RCP8.5) greenhouse gas concentrations and aerosols. Training data for the statistical downscaling model came from a validated dynamical downscaling of SAWs on a 10X10 km grid over SoCal (Chapter 2). SAWs were derived from downscaled GCM winds and compared to R1-derived SAWs over the common historical period. We thus validated the GCMs with respect to their ability to realistically

simulate annual SAW activity and its salient features: seasonality, frequency, intensity, and timing of extremes. We also assessed the sensitivity of SAWs to synoptic-scale PGF and further validated GCMs in this respect. This exercise did not yield clear winners among GCMs. In general, we found the ability of downscaled GCMs to represent SAWs to be reasonable overall, but some models displayed serious problems with specific features of SAWs. Nonetheless, the agreement between models on projected SAW changes was rather striking. We note that our study was limited to wind speed and direction only. The other salient features of SAWs – humidity and temperature – were not considered here. For winds, however, our results provide a consistent picture that provides important nuance heretofore unavailable.

Overall, GCMs agree on the gradual decrease in SAW activity, particularly in the shoulder seasons of fall and spring. The decrease in SAW activity is least pronounced during the winter peak of the SAW season. This decrease, which appears to be gradual, i.e. monotonic during the first and second halves of the 21st century, but not yet clearly evident in the 20th century, is driven by decreased PGF that is associated with SAWs. This result generally agrees with the conclusion of Hughes et al. (2011), who project decreased SAW frequency as a result of the greater warming projected over the Great Basin compared to that over the north-eastern Pacific Ocean. We further find that the decrease in SAW activity is driven most strongly and consistently by decreased frequency of SAWs, particularly in the shoulder seasons. Projected intensity, i.e. wind speed, also tends to decrease consistently, but to a much lesser degree. This is especially true for extreme SAWs, whose frequency is projected to decrease strongly (by 34±10%, i.e. mean±1sd) by the last half of the current century, but whose intensity is hardly projected to change.

A robust result that is salient for the timing of the wildfire season is that the SAW season is narrowing around its natural peak in December, when changes in SAW activity are projected to be minimal (-4% ±8% and -11% ±8%, for the first and second halves of the 21st century, respectively). November and January SAWs are also projected to become somewhat less active: by -5%±10% and -13%±11% in November, and by -12% ±5% and -18% ±5% in January. The strongest decreases in SAW activity are projected for the early SAW season (68% and 30%, respectively, on ensemble average for September and October in the second half of the century) and for the late season (35% in April and 50% in May). The expectation, therefore, is that climate change may result in a weakening contribution of SAWs to the traditional SoCal wildfire season's October peak. However, we may expect an increase in late-season, November-December-January, wildfires given the projected diminished decrease in SAW activity during this traditional peak of the SAW season and the independent projection of decreased fall precipitation (Pierce et al., 2013; Swain et al., 2018). Importantly, the intensity of extreme SAWs during the peak of the SAW season is not really expected to diminish. The slightly diminished SAWs (mainly in their frequency) in December, for example, will still tend to be stronger and more frequent in the late 21st century compared to historical SAWs in October, the historical peak of the wildfire season. In other words, the projected precipitation regime and SAW changes suggest a tendency for migration of the SoCal wildfire season peak from October towards December. Similar projected changes in precipitation and SAW regimes likely reflect the influence of poleward-expanding subtropical subsidence (Previdi & Liepert, 2007; Quan et al., 2014), which pushes synoptic activity, that drives both precipitation and SAWs, poleward, particularly in the shoulder seasons.

In light of these projections, the largest wildfire in SoCal history (Thomas Fire) occurring in December 2017 and fanned by back-to-back SAW events was a harbinger of wildfire seasonality we expect to experience more often in the future. In December, back-to-back SAWs are most probable providing opportunities for wildfires to burn longer and bigger. In the future, the probability of back-to-back events will diminish somewhat, but will still remain much stronger in December than it ever was in October or even November. The higher year-to-year precipitation volatility (Polade et al., 2014) translates into higher probability of extremely wet winters followed by extremely dry winters (Swain et al., 2018) and additionally suggests a boost to the availability of dry fuels, bolstering the later peak in future wildfire activity, i.e. nudging the extremes of future later fires to be more intense and, therefore, more extensive. On the other hand, the progressively less frequent SAWs in early-mid fall (September-October) would result in less fuel desiccation via SAWs themselves, which has yet to be quantified. Obviously, the above expectations about anthropogenically-driven changes in future wildfire activity need to be evaluated in a more robust framework involving precipitation and SAW projections including humidity and temperature, in addition to projected ecosystem changes, as well as population and WUI dynamics, all as comprehensive inputs into wildfire risk models. Such comprehensive models could then be used to test our hypotheses about the future of wildfire seasonality and dynamics in SoCal as well as to begin assessing future impacts of wildfires on society.

Acknowledgement. Authors conducted this work funded by University of California Office of the President MRPI grant MRP-17-446315 and the Climate Education Partners (www.sandiego.edu/climate), a NSF funded project DUE-1239797. CONACYT-UCMEXUS

doctoral fellowship (http://ucmexus.ucr.edu/) also contributed with financial support for Janin Guzman-Morales (scholar 214550). Additional support was provided by the California Energy Commission EPC-16-093 and the US Geological Survey grant G14AP00076. We thank Dan Cayan and David Pierce for stimulating discussions and CMIP5 for compiling and providing data from GCM simulations. Lastly, we would like to mention and honor the bright memory of Masao Kanamitsu, creator of CaRD10.

Chapters 3, in full, has been submitted for publication to *Geophysical Research Letters*, with slight modifications. Guzman-Morales, J., and Gershunov, A. (2018). Climate Change Suppresses the Santa Ana Winds of Southern California and Sharpens their Seasonality. *Submitted for publication in GRL*. The dissertation author was the primary investigator and author of this paper.

References

Delfino, R. J., Brummel, S., Wu, J., Stern, H., Ostro, B., Lipsett, M., … Gillen, D. L. (2009). The relationship of respiratory and cardiovascular hospital admissions to the southern California wildfires of 2003. Occupational and Environmental Medicine, 66(3), 189–197. https://doi.org/10.1136/oem.2008.041376

Gershunov, A., & Cayan, D. R. (2003). Heavy Daily Precipitation Frequency over the Contiguous United States: Sources of Climatic Variability and Seasonal Predictability. Journal of Climate, 16(16), 2752–2765. https://doi.org/10.1175/1520-0442(2003)016<2752:HDPFOT>2.0.CO;2

Guzman-Morales, J., Gershunov, A., Theiss, J., Li, H., & Cayan, D. (2016). Santa Ana Winds of Southern California: Their climatology, extremes, and behavior spanning six and a half decades. Geophysical Research Letters, 43(6), 2827–2834. https://doi.org/10.1002/2016GL067887

Hughes, M., & Hall, A. (2010). Local and synoptic mechanisms causing Southern California's Santa Ana winds. Climate Dynamics, 34(6), 847–857. https://doi.org/10.1007/s00382-009-0650-4

Hughes, M., Hall, A., & Kim, J. (2011). Human-induced changes in wind, temperature and relative humidity during Santa Ana events. Climatic Change, 109(S1), 119–132. https://doi.org/10.1007/s10584-011-0300-9

Jennings, M. K., Cayan, D., Kalansky, J., Pairis, A. D., Lawson, D. M., Syphard, A. D., … Vanderplank, S. (2018). San Diego County Ecosystems: Ecological Impacts of Climate Change on a Biodiversity Hotspots.

Jin, Y., Goulden, M. L., Faivre, N., Veraverbeke, S., Sun, F., Hall, A., … Randerson, J. T. (2015). Identification of two distinct fire regimes in Southern California: implications for economic impact and future change. Environmental Research Letters, 10(9), 94005. https://doi.org/10.1088/1748-9326/10/9/094005

Kalkstein, A. J., Kalkstein, L. S., Vanos, J. K., Eisenman, D. P., & Grady Dixon, P. (2018). Heat/mortality sensitivities in Los Angeles during winter: a unique phenomenon in the United States. Environmental Health, 17(1), 45. https://doi.org/10.1186/s12940-018-0389-7

Kalnay, E., Kanamitsu, M., Kistler, R., Collins, W., Deaven, D., Gandin, L., … Joseph, D. (1996). The NCEP/NCAR 40-Year Reanalysis Project. Bulletin of the American Meteorological Society, 77(3), 437–471. https://doi.org/10.1175/1520-0477(1996)077<0437:TNYRP>2.0.CO;2

Kanamaru, H., & Kanamitsu, M. (2007). Fifty-Seven-Year California Reanalysis Downscaling at 10 km (CaRD10). Part II: Comparison with North American Regional Reanalysis. Journal of Climate, 20(22), 5572–5592. https://doi.org/10.1175/2007JCLI1522.1

Kanamitsu, M., & Kanamaru, H. (2007). Fifty-Seven-Year California Reanalysis Downscaling at 10 km (CaRD10). Part I: System Detail and Validation with Observations. Journal of Climate, 20(22), 5553–5571. https://doi.org/10.1175/2007JCLI1482.1

Lynn, E., Andrew Schwarz, Jamie Anderson, & Matt Correa. (2015). Perspectives and Guidance for Climate Change Analysis. Climate Change Technical Advisory Group. Retrieved from http://climate.calcommons.org/bib/perspectives-and-guidance-climate-change-analysis

Meehl, G. A., Covey, C., Delworth, T., Latif, M., McAvaney, B., Mitchell, J. F. B., … Taylor, K. E. (2007). THE WCRP CMIP3 Multimodel Dataset: A New Era in Climate Change Research. Bulletin of the American Meteorological Society, 88(9), 1383–1394. https://doi.org/10.1175/BAMS-88-9-1383

Miller, N. L., & Schlegel, N. J. (2006). Climate change projected fire weather sensitivity: California Santa Ana wind occurrence. Geophysical Research Letters, 33(15), L15711. https://doi.org/10.1029/2006GL025808

Pierce, D. W., Das, T., Cayan, D. R., Maurer, E. P., Miller, N. L., Bao, Y., … Tyree, M. (2013). Probabilistic estimates of future changes in California temperature and precipitation

using statistical and dynamical downscaling. Climate Dynamics, 40(3–4), 839–856. https://doi.org/10.1007/s00382-012-1337-9

Polade, S. D., Pierce, D. W., Cayan, D. R., Gershunov, A., & Dettinger, M. D. (2014). The key role of dry days in changing regional climate and precipitation regimes. Scientific Reports, 4(1), 4364. https://doi.org/10.1038/srep04364

Polade, S. D., Gershunov, A., Cayan, D. R., Dettinger, M. D., & Pierce, D. W. (2017). Precipitation in a warming world: Assessing projected hydro-climate changes in California and other Mediterranean climate regions. Scientific Reports, 7(1), 10783. https://doi.org/10.1038/s41598-017-11285-y

Previdi, M., & Liepert, B. G. (2007). Annular modes and Hadley cell expansion under global warming. Geophysical Research Letters, 34(22), L22701. https://doi.org/10.1029/2007GL031243

Quan, X.-W., Hoerling, M. P., Perlwitz, J., Diaz, H. F., Xu, T., Quan, X.-W., … Xu, T. (2014). How Fast Are the Tropics Expanding? Journal of Climate, 27(5), 1999–2013. https://doi.org/10.1175/JCLI-D-13-00287.1

Syphard, A. D., & Keeley, J. E. (2015). Location, timing and extent of wildfire vary by cause of ignition. International Journal of Wildland Fire, 24(1), 37. https://doi.org/10.1071/WF14024

Taylor, K. E., Stouffer, R. J., Meehl, G. A., Taylor, K. E., Stouffer, R. J., & Meehl, G. A. (2012). An Overview of CMIP5 and the Experiment Design. Bulletin of the American Meteorological Society, 93(4), 485–498. https://doi.org/10.1175/BAMS-D-11-00094.1

Swain, D. L., Langenbrunner, B., Neelin, J. D., & Hall, A. (2018). Increasing precipitation volatility in twenty-first-century California. Nature Climate Change, 8(5), 427–433. https://doi.org/10.1038/s41558-018-0140-y

Yue, X., Mickley, L. J., & Logan, J. A. (2014). Projection of wildfire activity in southern California in the mid-twenty-first century. Climate Dynamics, 43(7–8), 1973–1991. https://doi.org/10.1007/s00382-013-2022-3